

Constraining the Interiors of Asteroids Through Close Encounters

Jack T. Dinsmore,^{1*} Julien de Wit²

¹*Department of Physics, Massachusetts Institute of Technology*

²*Department of Earth, Atmospheric, and Planetary Science, Massachusetts Institute of Technology*

Accepted XXX. Received YYY; in original form ZZZ

ABSTRACT

Knowledge of the interior density distribution of an asteroid can reveal its composition and constrain its evolutionary history. However, most asteroid observational techniques are not sensitive to interior properties. We investigate the interior constraints accessible through monitoring variations in angular velocity during a close encounter. We derive the equations of motion for a rigid asteroid’s orientation and angular velocity to arbitrary order and use them to generate synthetic angular velocity data for a representative asteroid on a close Earth encounter. Using Markov Chain Monte Carlo fits, we perform injection-retrieval tests on these synthetic data to gain insights into the extent to which interior properties can be constrained. We also perform a sensitivity analysis of such an inversion technique to asteroid parameters (e.g., moment of inertia and initial spin pole direction), observational set-up (e.g., measurement precision and cadence), and mapping models to convert constraints on the density moments to density distributions. We find that high precision in rotational period estimates (order of milliseconds to seconds) are necessary for each cadence, and that large asteroids (> 100 m radius) with low perigees (< 20 Earth radii) are necessary to resolve second-order density moments.

Key words: minor planets, asteroids: general – methods: data analysis

1 INTRODUCTION

Over the past twenty years, the increase in quantity and quality of sensitive all-sky surveys has prompted the discovery of numerous asteroids. Such advances have been made via ground-based surveys such as the Catalina Sky Survey [Larson et al. \(1998\)](#), Pan-STARRS [Kaiser et al. \(2002\)](#), and the Lincoln Near-Earth Asteroid Research project (LINEAR) [Stokes et al. \(2000\)](#), as well as space-based instruments such as the Wide-field Infrared Survey Explorer (WISE) mission [Wright et al. \(2010\)](#). Many of these asteroids are relatively small, but some are kilometre-sized and a few are predicted to closely encounter Earth or other planets in the near future. More encounter candidates are likely to be discovered by new efforts such as the Large-aperture Synoptic Survey Telescope (LSST) [Tyson \(2002\)](#). Their encounters can then be monitored by global ground-based networks such as the Las Cumbres Observatory (LCO) [Brown et al. \(2013\)](#). Such ground-based monitoring is typically used to derive the rotation period of an asteroid and its surface properties (see e.g. [Devogèle et al. \(2021\)](#)).

Since the tidal torque acting on an asteroid during an

encounter depends on the interior mass distribution, the careful monitoring of angular velocity variations during an encounter also presents a window into the interior properties of asteroids. The gravitational two-body system has been studied in the context of tidal torque to different orders and with several different methods [Paul \(1988\)](#); [Scheeres et al. \(2000\)](#); [Ashenbergs \(2007\)](#); [Boué & Laskar \(2009\)](#); [Hou et al. \(2017\)](#). Further studies showed that the tidal torque, observed through angular velocity perturbations, is sensitive to asteroid interior density distribution [Naidu & Margot \(2015\)](#); [Makarov et al. \(2022\)](#); [Scheeres et al. \(2004\)](#). However, density distribution features beyond the moment of inertia (MOI) ratios have not yet been extracted for any asteroid encounters. More research is needed to study in what cases these effects are observable, and what factors generally inhibit observation of these new features.

Angular velocity perturbations have been observed and used to extract asteroid properties in several cases, including for the 2013 encounter of (367943) Duende with Earth [Moskovitz et al. \(2020\)](#); [Benson et al. \(2020\)](#), and asteroid binaries (3905) Doppler and (617) Patroclus [Descamps et al. \(2020\)](#); [Berthier et al. \(2020\)](#). Orbital and physical properties, including MOI ratios have also been extracted for 99942 Apophis, which will closely encounter Earth in 2029 [Yu et al. \(2019\)](#).

* E-mail: jtd@stanford.edu

(2014); Hirabayashi et al. (2021); Valvano et al. (2022); Lee et al. (2022). It seems pivotal to augment previous work on the effect of tidal torque on Apophis’ angular velocity Souchay et al. (2014, 2018) so that upcoming observations may constrain these properties and thus improve our predictions.

We address this community need by developing a methodology to translate (1) time series of asteroid angular velocity data into constraints on density moments and (2) constraints on density moments into constraints on an asteroid’s density distribution. Other techniques, such as measurement of tidal distortion Richardson et al. (1998), impact or seismometry experiments Richardson et al. (2005), or gradiometry Carroll & Faber (2018), may additionally constrain the density distribution. In section 2, we introduce the analytical and numerical fundamentals of this methodology. There, we describe a simulation used to integrate the equations of motion and produce synthetic data of angular velocity over time, followed by a Markov Chain Monte Carlo (MCMC) fit process which extracts density moments from the fit data. We note that these equations of motion for an asteroid equation are novel and designed to be computationally efficient and valid to arbitrary order. We then describe three methods to generate full density distributions from the density moments. In section 3, we present the results of a series of injection-retrieval tests demonstrating the extent to which the properties of an asteroid chosen to generate synthetic spin data can be retrieved via our methodology. Finally, in section 4, we assess the sensitivity of these constraints to various physical, observational, and methodological parameters to provide guidance for monitoring upcoming close encounters. We also test the density distribution extraction methods on several sample asteroids.

2 METHODS

The only properties of an asteroid’s density moments that affect tidal torque interactions are its “density moments,” defined here as

$$K_{\ell m} = \frac{a_{\mathcal{A}}^{2-\ell}}{I_{\mathcal{A}}} \int_{\mathcal{A}} d^3 r \rho_{\mathcal{A}}(\mathbf{r}) R_{\ell m}(\mathbf{r}). \quad (1)$$

These are complex, unitless quantities. $\rho_{\mathcal{A}}(\mathbf{r})$ is the asteroid density distribution and $R_{\ell m}$ are the regular solid spherical harmonics (see appendix A for details). The integral is computed over the entire asteroid mass, denoted \mathcal{A} . $I_{\mathcal{A}}$ denotes a MOI scale defined as

$$I_{\mathcal{A}} = \int_{\mathcal{A}} d^3 r \rho_{\mathcal{A}}(\mathbf{r}) r^2 \quad (2)$$

while $a_{\mathcal{A}}$ is the length scale

$$a_{\mathcal{A}}^2 = \frac{1}{V_{\mathcal{A}}} \int_{\mathcal{A}} d^3 r r^2 \quad (3)$$

where $V_{\mathcal{A}}$ is the asteroid volume. We call these MOI and length scales in part because they obey $I_{\mathcal{A}} = \mu_{\mathcal{A}} a_{\mathcal{A}}^2$ where $\mu_{\mathcal{A}}$ is the mass of the asteroid for uniform asteroids. Note that $a_{\mathcal{A}}$ is a function only of the surface of the asteroid, so that $a_{\mathcal{A}}$ is known if the surface is observed.

The tidal torque experienced by an asteroid is

$$\begin{aligned} \boldsymbol{\tau} = & G \frac{I_{\mathcal{A}} I_{\mathcal{B}}}{2a_{\mathcal{A}}^2 a_{\mathcal{B}}^2} \left[\sum_{\ell m} a_{\mathcal{B}}^{\ell} J_{\ell m} \sum_{\ell' m'} a_{\mathcal{A}}^{\ell'} S_{\ell+\ell', m+m'}^*(\mathbf{D}) (-1)^{\ell'} \right. \\ & \times \sum_{m''=-\ell'}^{\ell'} \sqrt{\frac{(\ell'-m'')!(\ell'+m'')!}{(\ell'-m')!(\ell'+m')!}} \mathcal{D}_{m'm''}^{\ell'}(\alpha, \beta, \gamma)^* \\ & \times \left. ((i\hat{\mathbf{x}} - \hat{\mathbf{y}})(\ell'-m''+1) K_{\ell', m''-1} \right. \\ & \left. + (i\hat{\mathbf{x}} + \hat{\mathbf{y}})(\ell'+m''+1) K_{\ell', m''+1} + 2im'' \hat{\mathbf{z}} K_{\ell'm''}) \right], \end{aligned} \quad (4)$$

where \mathbf{D} is the position of the asteroid; α , β , and γ are $z-y-z$ Euler angles expressing the orientation of the asteroid; $S_{\ell m}$ are the irregular solid spherical harmonics; and $\mu_{\mathcal{B}}$ and $a_{\mathcal{B}}$ are the mass and radius of the central body while $J_{\ell m}$ are the density moments of the central body, with the a_{bulk} and a_{surf} of equation 1 replaced by $a_{\mathcal{B}}$. Equation 4 is derived in appendix A, assuming a rigid asteroid and no distant third-body perturbations.

Since it is the angular acceleration of the asteroid that is observable, rather than the torque applied, we also compute the MOI of the asteroid around the principal axes:

$$\begin{aligned} I_x &= \frac{2}{3} I_{\mathcal{A}} (K_{20} - 6K_{22} + 1) \\ I_y &= \frac{2}{3} I_{\mathcal{A}} (K_{20} + 6K_{22} + 1) \\ I_z &= \frac{2}{3} I_{\mathcal{A}} (-2K_{20} + 1). \end{aligned} \quad (5)$$

The angular acceleration of the asteroid is proportional to $\boldsymbol{\tau}/I$ (equation A14), such that the $I_{\mathcal{A}}$ factor of equation 4 is canceled out. Thus, the observables do not depend explicitly on $I_{\mathcal{A}}$, nor on the asteroid mass.

Throughout the paper, we refer to the “inertial frame” (the frame in which the orbit is fixed) and the “body-fixed frame” (the frame in which the asteroid is fixed and in which $K_{\ell m}$, $I_{\mathcal{A}}$, and $a_{\mathcal{A}}$ are computed), which are also defined in appendix A.

2.1 Simulation design

We built a publicly accessible, custom simulation in C++ to produce time series of angular velocity data during a close encounter with a central body. This simulation requires as initial data (1) the orbital parameters of the asteroid r_p (perigee distance) and v_{∞} (hyperbolic excess velocity); (2) the cadence of angular velocity observation Δt ; (3) the central body moments $J_{\ell m}$, mass $\mu_{\mathcal{B}}$, and radius $a_{\mathcal{B}}$; (4) the initial asteroid angular velocity in the inertial frame Ω_0 ; (5) the asteroid length $a_{\mathcal{A}}$ and (6) the asteroid’s density moments $K_{\ell m}$ and initial Euler angle γ_0 . All parameters except (6) are assumed to be known to high accuracy. For example, Ω_0 could be extracted from pre-encounter light-curve data and a_{surf} from a model for the asteroid’s surface using radar.

We assume for simplicity that the asteroid is initially not tumbling, though this assumption can be relaxed. We assume a short-axis rotation mode such that energy of the asteroid’s rotation is minimized. This sets $\beta = 0$ and we can further choose $\alpha = 0$. Only the Euler angle γ_0 is necessary to provide initial data for the simulation.

We begin our simulation at $D = 10r_p$, with velocity predicted by Kepler's laws given by the orbital parameters. Since the leading order of the equations of motion is $\ell' = 2, \ell = 0$, this corresponds roughly to a torque of 10^{-3} times the maximum torque at perigee. Unless otherwise indicated, the simulation is terminated at $D = 10r_p$ as well.

With the simulation inputs specified, the equations of motion are integrated via the Runge-Kutta fourth order method, with a variable time step

$$dt = dt_{\min} + 10^{-3}(dt_{\max} - dt_{\min}) \left[\left(\frac{D}{r_p} \right)^3 - 1 \right]. \quad (6)$$

The parameters dt_{\max} and dt_{\min} (20 and 10 seconds respectively) were chosen such that the numerical integration error was ~ 100 times the floating point error, and that neighbouring values of K_{3m} yielded significantly different spin pole data compared to floating point error. The data used to choose this dt was obtained using the reference asteroid configuration, described in appendix B.

2.2 Uncertainty model

To add noise to data generated via the above simulation, we use the following uncertainty model. Each asteroid spin vector Ω is assumed to be uncorrelated with other spin vectors, and we model uncertainty in the orientation and in the period as also uncorrelated. Consider a true spin vector Ω^* . For the sake of description, we work in coordinates in which $\Omega^* \parallel \hat{z}$. Then, expressing the observed spin vector Ω in spherical coordinates, we draw the polar angle from a normal distribution with standard deviation σ_θ centred on zero and the azimuthal angle from a uniform distribution. We also draw the ratio Ω/Ω^* from a log-normal distribution centred on one, with width σ_P/P , where $P = 2\pi\Omega$ is the period of the asteroid. Explicitly, the probability density function (PDF) of ρ is

$$P(\rho) = \frac{1}{\rho\sqrt{2\pi(\sigma_P/P)^2}} \exp\left(-\frac{\ln^2 \rho}{2(\sigma_P/P)^2}\right). \quad (7)$$

See figure 1 for an illustration of the uncertainty model. A log normal distribution is chosen such that $\rho > 0$, but since $\sigma_\rho \ll 1$ typically in our analysis, $P(\rho)$ is approximately Gaussian.

The log likelihood resulting from this uncertainty model is (excluding additive constants)

$$\ln \mathcal{L} = -\frac{1}{2} \sum_{i=0} \left[\frac{\cos^{-1}(\Omega_i^* \cdot \Omega_i / (\Omega_i^* \Omega_i))}{\sigma_\theta^2} + \frac{\ln(\Omega_i/\Omega_i^*)^2}{(\sigma_P/P)^2} + 2 \ln \frac{\Omega_i}{\Omega_i^*} \right]. \quad (8)$$

where Ω_i is the i th spin vector in the data set.

This model was chosen because it separates spin pole and period uncertainty. Therefore, if one is more precisely determined by measurement, σ_θ and σ_P/P can be adjusted separately in accordance.

2.3 Extracting density moments from spin data

Given synthetic data, an Affine Invariant MCMC Ensemble sampler was used to generate PPDs from flat priors. We use

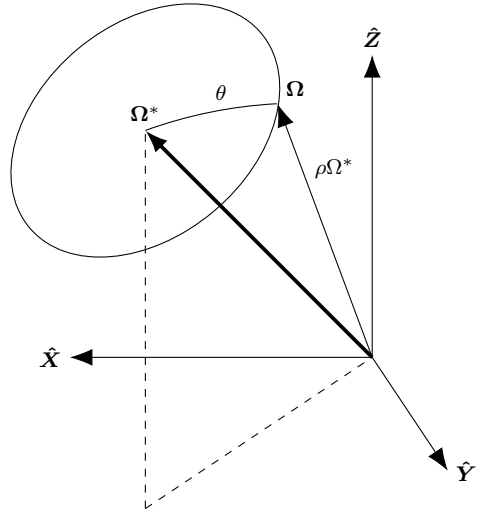


Figure 1. Diagram in the inertial frame of the uncertainty model used to define the probability that the true spin vector Ω^* should be observed as Ω . The parameter θ is drawn from a Gaussian with width σ_θ , and ρ is drawn from a log normal distribution with width σ_ρ .

the Python implementation `emcee` Foreman-Mackey et al. (2013). Our parameters were γ_0 , K_{20} , K_{22} , and K_{3m} (10 in total), and were bounded by $|\gamma_0| < \pi/4$, and bounds on K_{2m} given in equation A5. Note that γ_0 is degenerate with $\gamma_0 + \pi/2$ because both of these align the asteroid principal axes with the body-fixed axes. The other bounds were $|K_{3m}| < 1$. In general, spin data is most sensitive to γ_0 and K_{2m} , which we call the “first-order parameters.” We call K_{3m} the “second-order parameters.”

The MCMC was determined to converge when the fractional change in autocorrelation time (computed every 100 iterations) was one percent, and the number of iterations computed so far was more than 100 times the autocorrelation time. The MCMC fit also was set to terminate if more than 10^5 iterations were run, but this only occurred for fits in which the data quality was low, leading to degeneracies between the second order parameters (K_{3m}). This degeneracy could be removed by only fitting K_{2m} instead. About 10^4 iterations was often sufficient, which generally consumed about 7 hours of computation time on a super computer running 16 threads on 8 cores.

Before the MCMC was run, local minima in the likelihood were found via the Nelder-Mead algorithm implemented in `scipy` Gao & Han (2012). Generally, only one local minimum existed, except when $K_{22} = 0$ in which case rotational symmetry caused multiple values of γ_0 to be degenerate. Ensemble walkers were initialized near this local minimum, distributed by a Gaussian approximation of the likelihood, as determined via the Hessian of the likelihood at the minimum. Due to the high sensitivity of the angular velocity data to density moments, the minimization procedure sometimes failed to isolate the minimum likelihood. Therefore, a simpler simulation without the K_{3m} terms of equation 4 was first used to minimize likelihood as a function of the first-order parameters γ_0 and K_{2m} , and then the full simulation was used to find the second-order parameters K_{3m} with the first-order parameters fixed.

To further ensure convergence, we minimized with respect to data truncated after perigee at double the perigee distance. This cut-off was manually chosen. The minimum was then further refined by minimizing based on the full data, with the previous minimum as the initial estimate.

2.4 Density distribution constraints

The asteroid density distribution $\rho_A(\mathbf{r})$ is not uniquely constrained via tidal torque interactions because only the density moments $K_{\ell m}$ contribute to equation 4. For example, since the mass of the asteroid is unconstrained, $\rho_A(\mathbf{r})$ cannot be determined on an absolute scale. However, by making sufficient assumptions about the density distribution, we can nevertheless extract fluctuations in $\rho_A(\mathbf{r})$ across the asteroid from $K_{\ell m}$. To best understand the potential density distribution of an asteroid, an ensemble of models with differing assumptions is desired, so that common traits across the models can be identified. To this end, we thoroughly outline two possible models and discuss two more in appendix ??.

We assume that the asteroid's surface is known in the inertial frame from radar data. Since the asteroid tumbles during the encounter, we also assume that the center of mass of the asteroid is extracted. However, the density moments which are extracted from flyby data are known instead in the body-fixed frame.

We rotate the known surface of the asteroid to a new frame called the “hybrid frame” by translating such that the known center of mass is at the origin, then rotating such that Ω_0 points in the $+\hat{\mathbf{z}}_{\text{hybrid}}$ direction and $\hat{\mathbf{Y}}$ points in the $\hat{\mathbf{Y}}_{\text{hybrid}}$ direction. Since Ω_0 is exact, the surface in this hybrid frame is known exactly. The hybrid frame differs from the body-fixed frame only by a rotation around $\hat{\mathbf{z}}_{\text{hybrid}}$ of γ_0 . Such rotations affect density moments via

$$K_{\ell m}^{\text{hybrid}} = e^{-im\gamma_0} K_{\ell m}^{\text{body-fixed}}. \quad (9)$$

by equation A9. Thus, uncertainty on $K_{\ell m}^{\text{body-fixed}}$ (obtained from the encounter data) can be translated to uncertainty in $K_{\ell m}^{\text{hybrid}}$. Henceforth, we will operate only in the hybrid frame and suppress the label.

When the K_{3m} are extracted, 15 moments are known (excluding K_{00}). Since the asteroid mass cannot be determined by this analysis, it is convenient to additionally set the mass equal to its volume, so that the average density is one and thus the extracted densities can be interpreted as ratios of ρ/ρ_{avg} . Three more moments are redundant with the center of mass, such that only twelve finite elements are free. In cases where γ_0 is known very accurately such that the correction imposed by equation 9 is very small, it is numerically favourable not to impose this equation on K_{2m} . In this case, the three orientation constraints that set $K_{21} = \Im K_{22} = 0$ carry over to the hybrid frame so that there are nine degrees of freedom (DOF). Since γ_0 is precisely known for all cases studied in this paper, we will always study this case. We also place additional constraints that $0.25 < \rho < 3$ to ensure realistic densities.

To extract a density distribution, we use another MCMC given one of the two parametrizations of density distributions discussed below. The prior is set to be flat and nonzero for all configurations that obey the $0.25 < \rho < 3$ constraint. The likelihood used is set equal to the

multivariate-Gaussian approximation of the posterior distribution for $K_{\ell m}$, extracted from flyby data. Otherwise, the MCMC parameters chosen were identical to those discussed in section 2.3. We also present two further models in appendix C which are viable substitutes for the following two models but are not used in the main text.

2.4.1 Finite element model

Given values of $K_{\ell m}^{\text{body-fixed}}$ and their uncertainties extracted from encounter data, there are many ways to extract a density distribution. Here, we outline a method termed the “finite element” model. We divide the asteroid into N finite elements of uniform density and use the density ρ_i of each as parameters. The four constraints imposed by the known mass and center of mass of the asteroid (seven with K_{21} and $\Im K_{22}$ are also fixed) are used to constrain some of these ρ_i . The constrained densities are easily computed since the asteroid mass μ_A and the product $I_A K_{\ell m}$ are both linear functions of ρ_i . Because $K_{\ell m} = 0$ implies that $I_A K_{\ell m} = 0$, computing the constrained densities is simply a matrix inversion.

The size and location of the elements must be chosen before extracting their densities. Best results generally require elements of equal size to be chosen. To remove the dependence on this choice, density distributions for many distinct element layouts can be extracted and the density of each point in the asteroid can be randomly sampled from any of these solutions to yield estimates for the mean density and uncertainty in density at each point.

The value of N must be carefully chosen, since it embodies a balance between the precision and accuracy of the resulting distribution. If N is set equal to the number of data points, an accurate solution is guaranteed, but uncertainties are inflated. If N is chosen lower, the choice of element layout might exclude a distribution that exactly matches $K_{\ell m}$, but uncertainties are diminished due to less redundancy in the model. An analysis of which value of N is appropriate for our purposes is given in section 4.3.

2.4.2 Lumpy model

A drawback of the finite element model is that the generated density distribution might not be representative of the asteroid if the elements are not optimally placed. We therefore describe an alternate model, which includes the positions of the elements as parameters at the cost of larger elements and therefore lower resolution. We call this model the “lumpy” model.

Suppose the asteroid is formed of N constant-density, possibly overlapping “lumps,” enclosed within a constant-density substrate whose surface is visible to observers. The lumps and the substrate are described by the mass added to the substrate by a lump μ_i , the position of its center of mass \mathbf{r}_i (relative to the asteroid's center of mass), its density moments $K_{\ell m}^{(i)}$, and its length scale a_i . Here, i denotes the index of the lump where the substrate is $i = 0$. We do not need to include I_i as a free parameter because these lumps have constant density, so that $I_i = \mu_i a_i^2$. Furthermore, by requiring that a lump's density moments be computed relative to the center of mass of the lump, we have $K_{1m} = 0$.

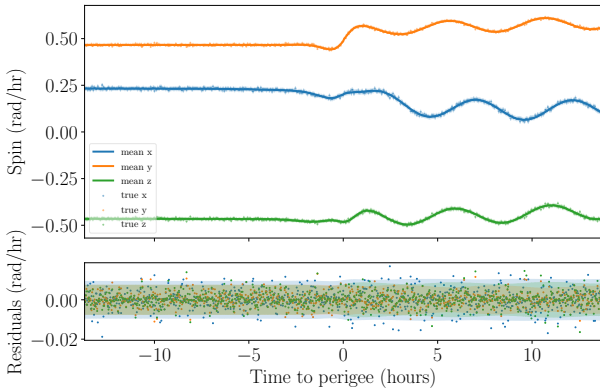


Figure 2. Data, best-fitting results, and residuals for a fit to synthetic data simulated for an asymmetric reference asteroid. Uncertainty bands are also shown. The best fit results appear consistent with the data.

The translation rules of spherical harmonics give that the asteroid properties in the hybrid frame are

$$K_{\ell m} = \left[\sum_{i=0}^N \frac{a_i^2 + r_i^2}{a_A^2} \mu_i \right]^{-1} \times \left[\sum_{i=0}^N \sum_{\ell' m'} \mu_i \frac{a_i^{\ell'}}{a_A^\ell} R_{\ell-\ell', m-m'}(\mathbf{r}_i) K_{\ell' m'}^{(i)} \right] \quad (10)$$

where the sum limits are $0 \leq \ell' \leq l$ and $-\ell' \leq m' \leq \ell'$. We also have total mass and center of mass constraints:

$$\mu_A = \sum_{i=0}^N \mu_i, \quad 0 = \sum_{i=0}^N \mu_i \mathbf{r}_i. \quad (11)$$

Additional constraints can be imposed on $K_{\ell m}^{(i)}$ if desired. For example, we can require that the lumps be ellipsoids, so that $K_{3m}^{(i)} = 0$. Additional rotational symmetries also constrain K , with the most extreme case being that spherical lumps have $K_{\ell m} = 0$ for $\ell > 0$. However, $K_{00} = 1$ is guaranteed by definition, meaning that each spherical lump has only five DOF (a_i , μ_i , and \mathbf{r}_i). The substrate has one degree of freedom, since only μ_0 is unknown. Thus, this lumpy model has $5N - 3$ total DOF. Again, the choice of N affects the accuracy and uncertainty of the model results, which is discussed in section 4.4.

3 RESULTS

To demonstrate our interior-probing methodology, we provide a full density distribution retrieval applied to synthetic data for the asymmetric reference asteroid. We first introduce the retrieval capabilities regarding density moments, then we turn to the constraints that can be derived reliably on the density distribution. For both level of information retrieval, we find that the results are consistent with the properties used to generate the synthetic data.

3.1 Density moments

Figure 2 shows our synthetic spin data. The best-fitting model is overlaid in the top panel and residuals are shown

the bottom panel. Uncertainties are plotted on the residuals corresponding to the square root of the diagonal entries of the covariance matrix (correlations not included). The fit results are clearly consistent with the data. This figure is also instructing in revealing which points in the data set are most informative. The at-perigee data is irregular and reveals information about the density moments, and the post-perigee data shows torque-free tumbling behaviour which constrains K_{2m} via the moment of inertia ratios, and also indirectly sheds light on the at-perigee data by constraining the rotational velocity the asteroid must have had when leaving the perigee.

Figure 3 shows a corner plot of the PPDs of the ten parameters (namely γ_0 and $K_{\ell m}$ for $\ell \leq 3$), marginalized to functions of one (histograms) or two (contours) variables. The true parameters are shown as lines. Note that the true parameters usually lie within 1 or 2σ of the $\Delta K_{\ell m} = 0$, where $\Delta K_{\ell m}$ is the difference between the posterior $K_{\ell m}$ and the true $K_{\ell m}$. The PPDs are generally Gaussian and sometimes show correlation between parameters, but no continuous degeneracy occurs. We performed 48 independent minimizations of the likelihood before the MCMC fit began, each with an initial point chosen randomly in the parameter space. All converged to the same minimum, demonstrating that the model lacks discrete degeneracy as well.

3.2 Density distribution

Density moments of the kind described above were extracted for the asymmetric and symmetric reference asteroids. The finite element model was then used to extract density distributions from these moments, and propagate uncertainties. Five DOF were used rather than the maximum possible number of nine, and 20 different finite element layouts were used to generate sample density distributions to avoid dependence on the manually-chosen layout. The resulting density distributions and uncertainties are displayed in figure ??.

The figure demonstrates that the finite element model successfully extracts density distributions consistent with the extracted density moments, as shown by the χ^2 value per degree of freedom, χ_r^2 , depicted in the figure. These express the agreement of the density moments of the shown distributions with the posterior distributions for the density moments, produced by the MCMC described in section 2.3. $\chi_r^2 = 0$ indicates that the moments of the shown distributions are exactly equal to the means of the moment posterior extracted by the MCMC. The accuracy of this model is robust for additional shapes, including non-ellipsoidal shapes.

Furthermore, the finite element density distributions are consistent with uniform, which is the true density distribution of the asteroid. For the reference asteroid observational set-up, the uncertainty on observations is such that the density distribution is generally within 10% of the true density (second column) while the density uncertainty is generally less than 40-50% of the density value at any point in the asteroid (third column). The dependence of this constraint on the observational set-up is discussed in section 4.1. In no place is the significance of these deviations from the true distribution greater than 0.3σ (last column).

The lumpy model also yields distributions which are consistent with the extracted moments and consistent with

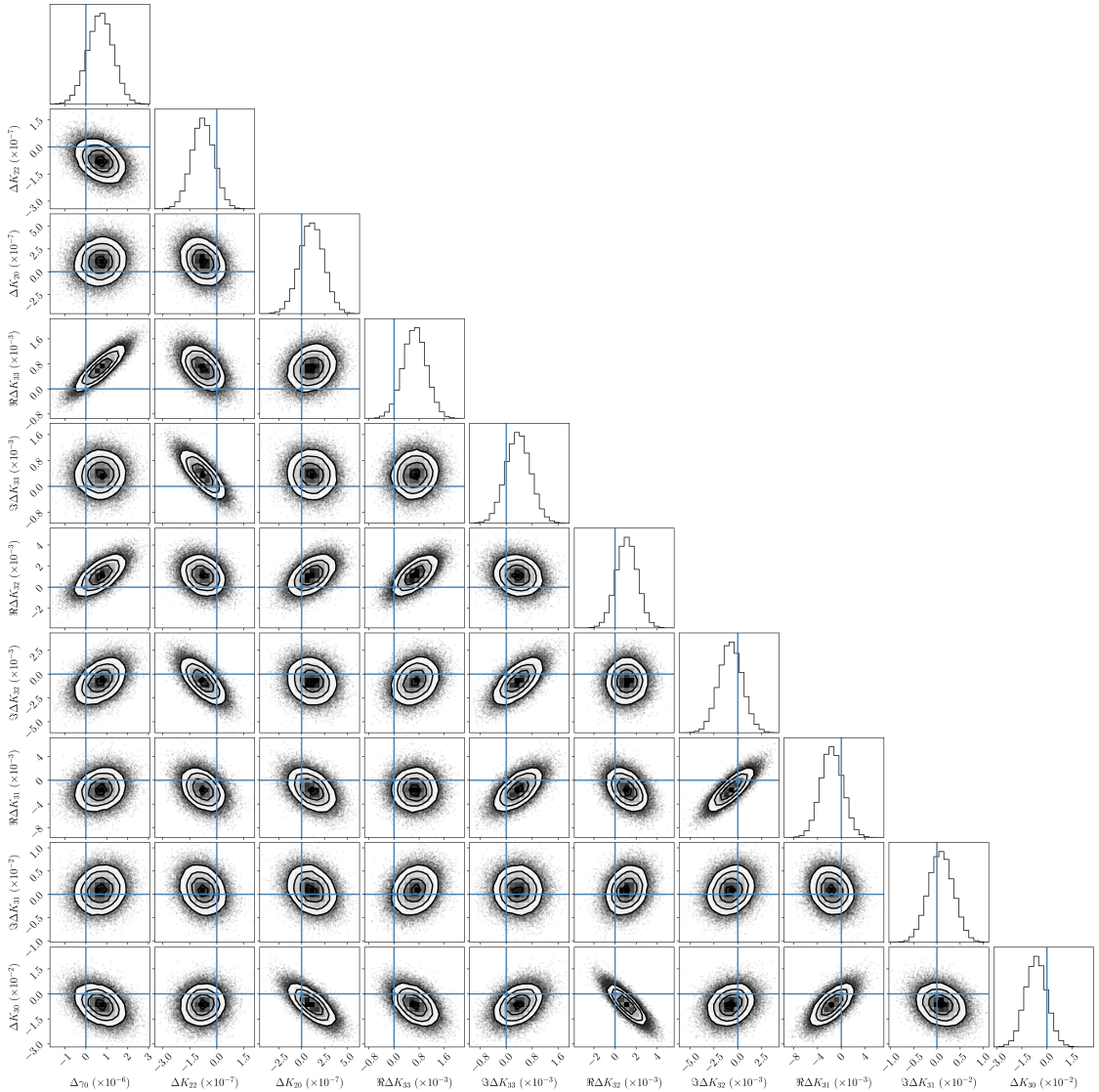


Figure 3. PPDs extracted from synthetic encounter data for the asymmetric reference asteroid. Samples from the MCMC fit are shown as individual points, and the contours enclose 1, 2, and 3σ confidence regions. True values are shown as blue lines. PPDs are Gaussian and show no degeneracies.

uniform. These distributions have much lower uncertainty than the finite element distributions (maximum uncertainty on the order of **JTD: number**) due to its few degrees of freedom. With only one lump, the location of the known center of mass requires that the lump lie at the centroid of the asteroid center with mass close to zero and unconstrained radius. Hence, the uncertainty of regions far from the asteroid is typically very small, while regions close to the center are more apt to be contained inside a lump. In order for the lumpy model to converge given the unconstrained lump radius, we use the mass-weighted $\mu_i a_i \rightarrow 0$ as a model parameter rather than the lump length a_i .

We also explore model behaviour in non-uniform density asteroids. We employ an asteroid of the same shape as the asymmetric asteroid, and in the same flyby scenario, but we place a solid core of radius 500 m and density three times the surrounding density at the center of the asteroid.

This changes the asteroid density moments. New density moments are extracted via the process described in section 2.3 and the finite-element and lumpy models are used to extract density distributions shown in figure ??.

Once again, figure ?? shows that the model results are successful in that they reproduce the extracted density moments (χ^2_r is low). However, the density distributions extracted by the finite model match the true distributions less well. The deviation the true density extends to as much as 35% in some locations, leading to a maximum significance of 0.86σ . The distributions are consistent with the true distribution, but the finite element model has distributed the core into the rest of the asteroid so that the peak density is lowered.

However, the lumpy model is designed to detect discrete changes in density distribution, and identifies the boundary of the core very accurately. Deviations from the truth are

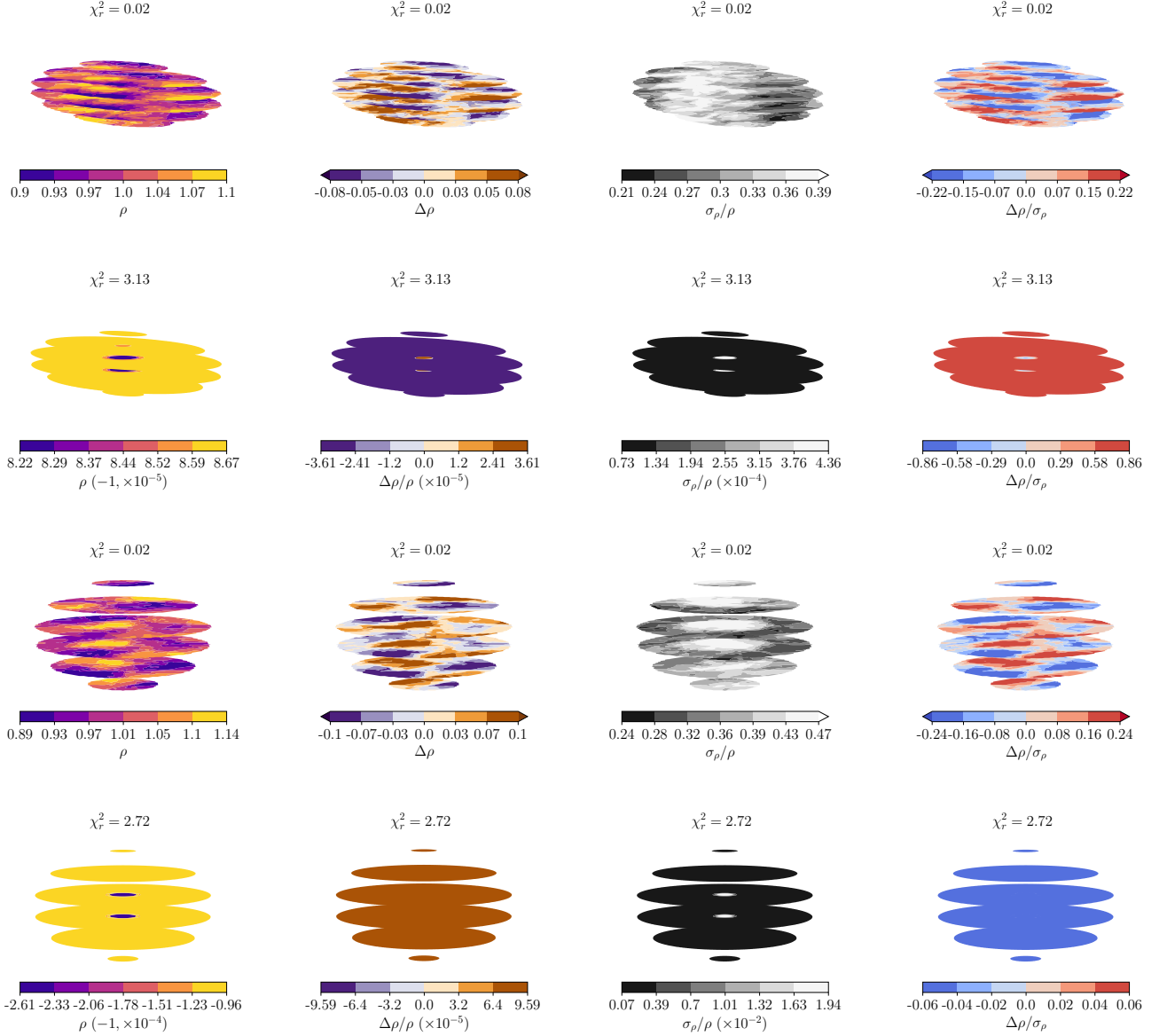


Figure 4. Cross-sectional slices of the density distributions extracted via the finite element model for the asymmetric (*first and third row*) and symmetric (*second and fourth rows*) reference asteroids. The finite element model (*top two rows*) and the lumpy model (*bottom two rows*) are employed. From left to right, the densities, deviations from the true density, uncertainties, and significance of the deviations are plotted. These figures are available in animated form in appendix figure F1. Extracted densities are generally within 10% of the truth.

less than 0.2%, with uncertainties about 10% of the local density at maximum and usually much lower. The significance of the deviations is around 20%, as it was in figure ?? where the extracted distribution again matched the truth. The low uncertainty is caused by the small number of degrees of freedom (2) of the lumpy model. A consequence is that if the core had been non-spherical, the lumpy model would be inaccurate, with significant deviations from the truth. Therefore, neither model is more correct in the general case, but each can be used to explore different scenarios.

4 DISCUSSION

4.1 Dependence of uncertainty on encounter properties

The question of which encounters are most suited to this methodology is of great interest, as is the question of how observational campaigns can be designed to best take advantage of an asteroid to maximize the success of this methodology. We investigate a mix of encounter parameters, from observational parameters (the data uncertainty, the cadence of observations, and gaps in data coverage) and physical asteroid properties (the encounter's orbital properties, the asteroid's true shape, and its initial rotational velocity), and

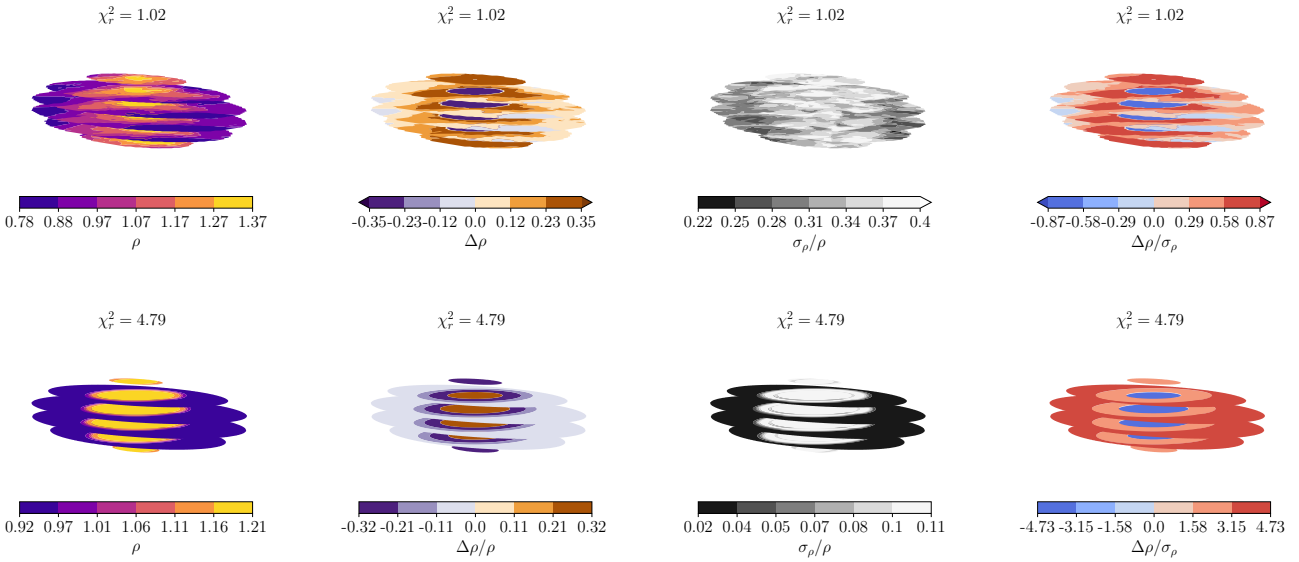


Figure 5. Cross-sectional slices of the density distributions extracted via the finite-element (*top*) and lumpy (*bottom*) models for an asteroid with a centred core. From left to right, the densities, deviations from the true density, uncertainties, and significance of the deviations are plotted. These figures are available in animated form in appendix figure ???. The core is successfully extracted in all cases.

discuss their effect on the uncertainty of this methodology’s results.

We study both the uncertainties on the density moments and uncertainty on density distribution. Moment uncertainty $\sigma(K_{\ell m})$ is defined as the range of $K_{\ell m}$ values that contains 68.27% of the marginal PPD for each ℓ and m . Since there is no degeneracy between moments and the actual encounter data, this uncertainty is well-defined. However, its physical relevance is not obvious. The density distribution uncertainty σ_ρ/ρ is defined as a map of uncertainty over the asteroid, made by taking the standard deviation of density at each point over 5000 maps of asteroid density, each made using a different sample of the output of the density distribution MCMC described in section 2.4. The median uncertainty over this map, divided by the local density, is taken to represent the density distribution uncertainty. This measure of uncertainty is more physically relevant than moment uncertainty, but it is strongly dependent by choices of the density distribution model, degrees of freedom, prior constraints, and other effects unrelated to the encounter properties. We therefore investigate both the moment uncertainty and the density distribution uncertainty.

Table 1 displays the encounter properties which beyond which the density distribution uncertainty rises above two sample values we term the “weak” and “strong” thresholds. These values are $\sigma_\rho/\rho = 10^{-4}$ (weak) and 10^{-3} (strong), for density distributions extracted via the lumpy model. These thresholds are manually chosen, and adjustments to them or to the lumpy model will affect the data of table 1. Figure 6 depicts the same σ_ρ/ρ as a function of initial spin pole direction, while figure 7 depicts σ_ρ/ρ as a function of the encounter properties. Both highlight the threshold values of table 1 with red lines. Bands contain 68% (light) and 95% (dark) of the density uncertainty over the asteroid are shown for figure 7.

Table 1 reveals that the most limiting physical proper-

Encounter property	Weak	Strong
Perigee (r_p , Earth radii)	<6.0	<18
Excess velocity (v_∞)	-	-
Asteroid length (a_A , m)	>15	-
Period (P_ω , hr)	>7.6	-
Spin period uncertainty (σ_P , ms)	<12	<270
Spin pole uncertainty (σ_θ , °)	<1.9	<35
Cadence (Δt , min)	<15	-
Data gap (T_{gap} , hr)	-	-

Table 1. The weak and strong thresholds on physical / observational properties (*top* / *bottom*) consistent with useable density distribution uncertainty. Perigee and observational uncertainty are the most constraining properties, followed by rotational period, asteroid length, and observational cadence.

ties of the asteroid are its perigee and period. Excess velocity does not greatly affect the uncertainty of the density distribution, and asteroid length is only effective for $a_A \sim 15$ m. By contrast, the radius of asteroid 99942 Apophis is ~ 300 m and Apophis will encounter Earth in 2029. Apophis’s perigee of 5–6 Earth radii also obeys the weak and strong constraints. In addition to the period constraint shown in this table, figure 6 also shows a threshold on spin pole direction. **JTD: Describe**.

Table 1 also demonstrates the strong affect of properties of the observational campaign on the final density uncertainty. Most vital are the uncertainty on the instantaneous asteroid rotational period σ_P/P and its direction σ_θ , which require precision on the order of tens to hundreds of milliseconds and degrees every cadence, respectively. This could be accomplished by multiple, precise angular velocity measurements from multiple telescopes, or by increasing the time between observations to maximize the change in period between observations. Increasing the data set size to include more post-flyby tumbling data would also relieve the burden on each data point for uncertainty to be so low. On the

Figure 6. Median ratio of density uncertainty to density computed over the reference asteroid density distribution via the lumpy model as a function of initial spin pole direction. The benchmark uncertainty thresholds (red lines) are shown, as is the reference spin pole direction ([JTD: What symbol?](#)). [JTD: Summary](#)

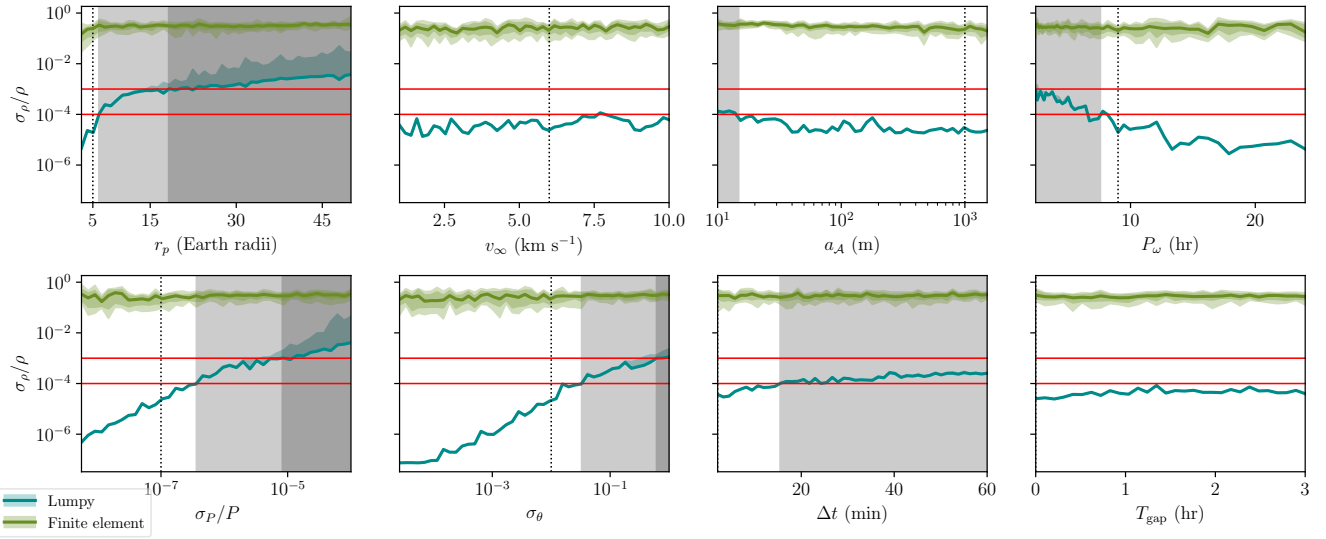


Figure 7. Median ratio of density uncertainty to density computed over the reference asteroid density distribution as a function of physical / observational encounter properties (top / bottom). Density distributions from both the lumpy and finite element models are used. The benchmark uncertainty thresholds (red lines) are shown and the properties that exceed these thresholds are shaded. Te vertical black dotted lines are the property values of the reference asteroid. The figures illustrate the marked difference in density distributions that results from using different models.

other hand, the cadence of observations Δt and the presence of gaps in the data T_{gap} do not affect results as strongly. Observations can be as much as 15 minutes apart to obey the weak threshold, with no constraint required to meet the strong threshold in our data set (which contains $\Delta t < 1$ hr). Likewise, there is no constraint on our data set of $T_{\text{gap}} < 3$ hr. This gap was simulated to occur in one contiguous unit centred on the encounter perigee, where torque is highest. If the gap occurred elsewhere in the data set or was subdivided into multiple gaps, it would likely affect density uncertainty even less. All of these thresholds are liable to change if the encounter properties are adjusted, since they are all inter-dependent.

Figure 7 reveals that the thresholds presented in table 1 are particularly sharp (a steep slope of σ_ρ/ρ) for the encounter perigee r_p and observational precision σ_P and σ_θ . These thresholds are therefore less likely to change if the asteroid properties are altered, whereas the thresholds on period P_ω , length a_A , and cadence Δt are much more volatile. The figure also displays the stark difference between density uncertainty as computed by the lumpy model and the finite element model. This is partially due to different choices in the number of DOF (5 for the finite element model and 2 for the lumpy model). The model assumptions also affect this uncertainty; the lumpy model must place the asteroid lump at the center of the asteroid since placing it elsewhere would move the asteroid's center of mass away from its observed position. Therefore, uncertainty on the edge of the asteroid where the lump is unlikely to be located, is very low for the lumpy model. The same reasoning does not apply to the finite element model, which has no bias towards the asteroid

center. This model-dependence of σ_ρ/ρ is another reason to take the thresholds of table 1 as estimates rather than strict limits on encounter properties.

To address the dependence of σ_ρ/ρ on the choice of model, we investigate moment uncertainty as well. Figures ?? and ?? display moment uncertainty $\sigma(K_{\ell m})$ on physical and observational encounter properties respectively. The thresholds of table 1 are depicted as red lines. Also shown is moment uncertainty as a function of K_{2m} in figure 10.

Figure ?? reveals that σ_ρ/ρ is more sensitive to $\sigma(K_{2m})$ than to K_{3m} . For instance, $\sigma(K_{2m})$ is constant as a_A is varied despite a dramatic increase in $\sigma(K_{3m})$ for low a_A . The resulting σ_ρ/ρ is mostly constant. However, the roles are reversed for P_ω , where $\sigma(K_{3m})$ (except for $m = 0$) are mostly constant, and here σ_ρ/ρ follows the trend of $\sigma(K_{2m})$ and increases for low rotational period. This fact has several consequences. First of all, if more post-flyby tumbling data is collected, this will place stronger constraints on K_{2m} and not K_{3m} . If so much data is available that K_{2m} have essentially no uncertainty, then uncertainty on K_{3m} will be dominant and the most constraining parameters will change. Rotational period P_ω will cease to be a vital parameter but asteroid length a_A will be because $\sigma(K_{3m})$ are much more dependent on a_A than P_ω .

Figure 8 also demonstrates exponentially increasing $\sigma(K_{\ell m})$ as a function of perigee r_p , indicating that the constraint on r_p noted in table 1 is not entirely a feature of the density model. (Figure 7 also indicated this, since σ_ρ/ρ falls for low perigee in both the lumpy and the finite element model). Dependence of moment uncertainty on data precision σ_P and σ_θ is similarly exponential as shown by figure

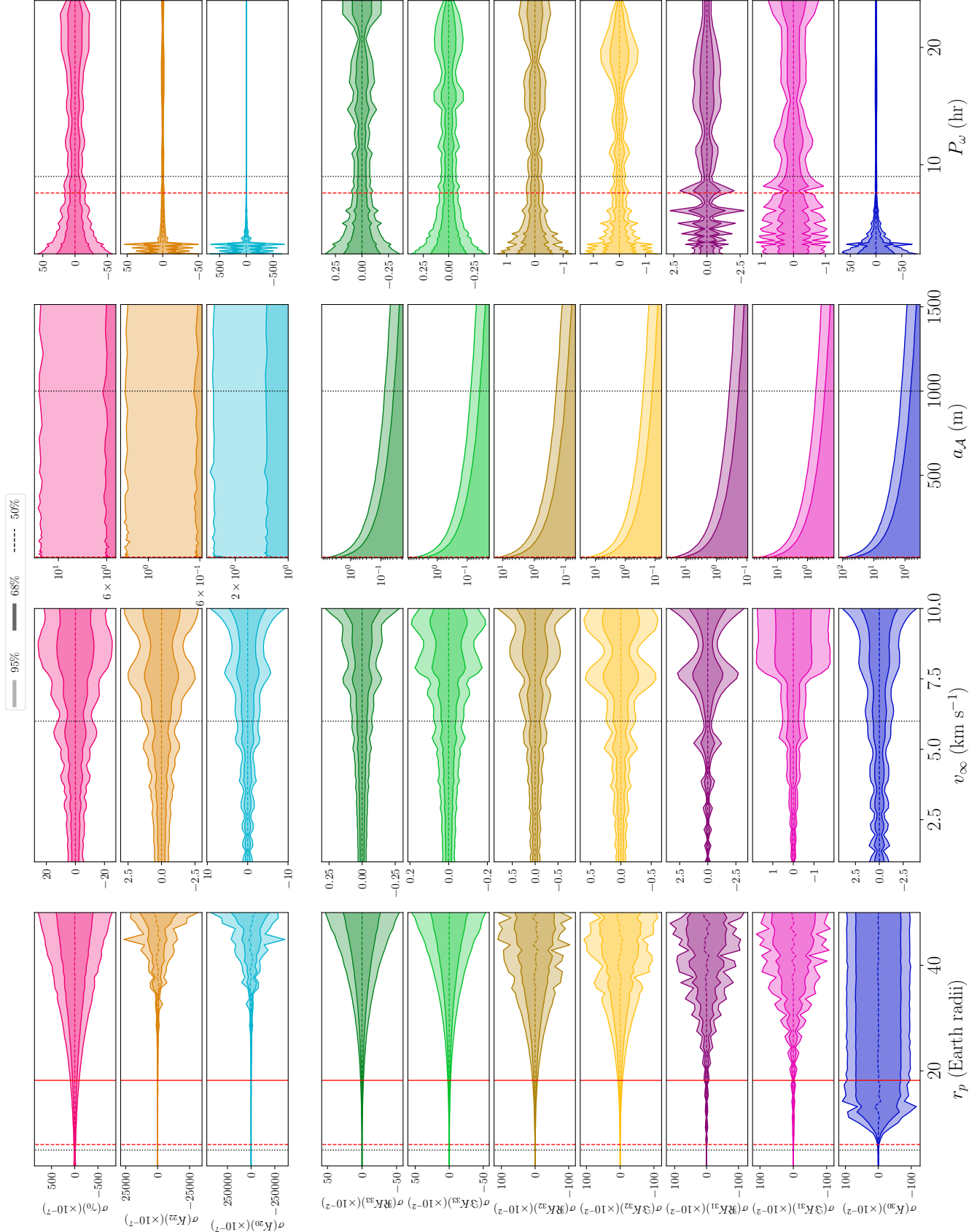


Figure 8. 1 and 2σ confidence intervals for the first-order parameter PPDs (*top*) and second-order parameters (*bottom*) as a function of (left to right) perigee, excess velocity, spin pole uncertainty, and period uncertainty. The vertical dashed line indicates the reference asteroid values. The red vertical lines indicate when $\sigma(K_{3m}) = 0.01$.

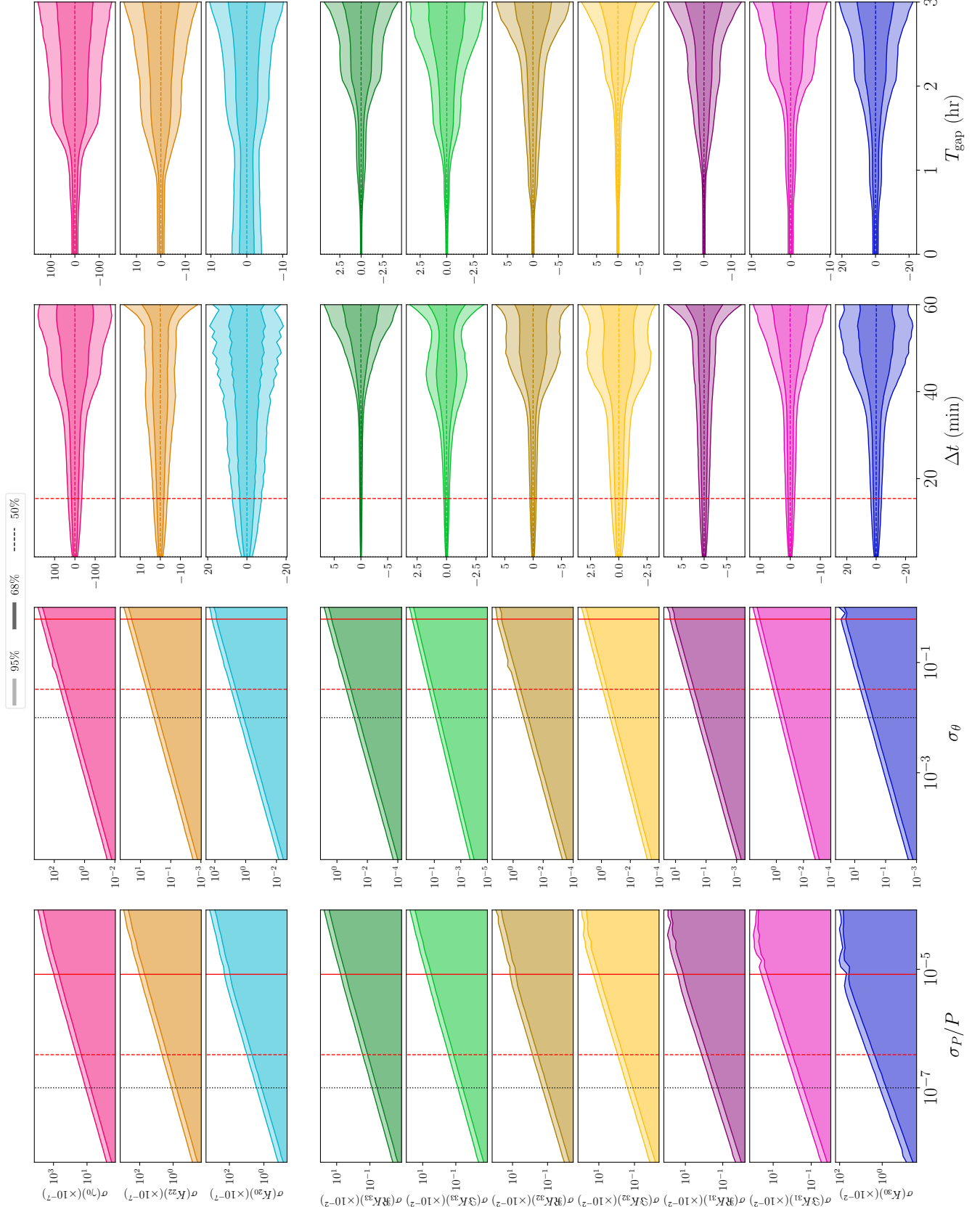


Figure 9. 1 and 2σ confidence intervals for the first-order parameter PPDs (*top*) and second-order parameters (*bottom*) as a function of (left to right) asteroid length, observational cadence, data gap at perigee, and rotational period. The vertical dashed line indicates the reference asteroid values. The red vertical lines indicate when $\sigma(K_{3m}) = 0.01$.

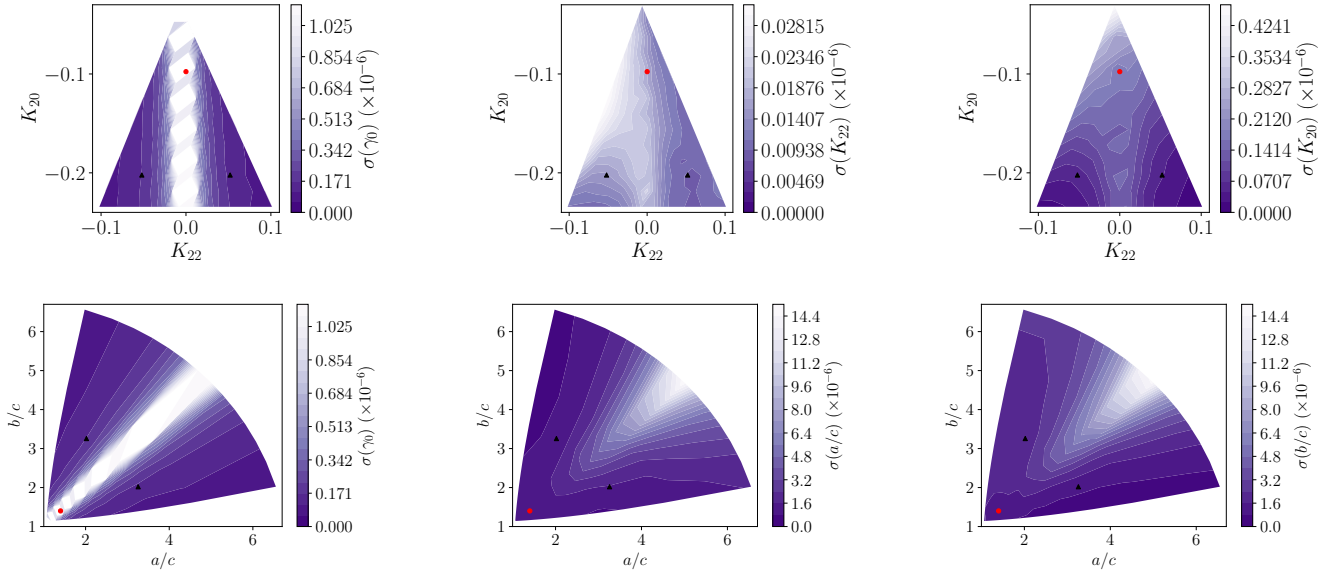


Figure 10. 1σ posterior uncertainty for first-order parameters γ_0 , K_{22} , and K_{20} (top row) and γ_0 , a/c , and b/c (bottom row). Also shown as black points are the reference asteroid shapes: symmetric (red circle) and asymmetric (black triangle). Symmetric asteroids ($K_{22} = 0$ or $a/c = b/c$) show increased posterior uncertainty, but otherwise posterior uncertainty is roughly constant.

9. However, moment uncertainty on cadence Δt and gaps in data T_{gap} are less exponential. These tend to increase in uncertainty at some characteristic time scale of $\Delta t \sim 15 - 40$ min for cadence and 1 – 2 hr for T_{gap} . As long as Δt and T_{gap} are below these time scales, uncertainty is not strongly dependent on them.

Finally, figure 10 depicts moment uncertainty $\sigma(K_{2m})$ as a function of K_{2m} and γ_0 . K_{2m} can be interpreted as moment inertia ratios or the dimensions of the uniform-density ellipsoid with the same $K_{\ell m}$. Therefore, moment uncertainty is depicted both as a function of K_{2m} and these ratios a/c and b/c . The figure shows a dramatic increase in moment uncertainty for $K_{22} = 0$, which corresponds to $a = b$, or a rotationally symmetric ellipsoid. This uncertainty is caused by degeneracy in the model; if the asteroid is rotationally symmetric, then two principal axes can lie anywhere in the xy -plane, so that the definition of γ_0 becomes meaningless. γ_0 is therefore poorly constrained as $K_{22} \rightarrow 0$. Figure ?? revealed that density distributions can still be extracted for symmetric asteroids, but to reduce uncertainty, the moments must be re-parametrized to remove this degeneracy if this methodology is to be run on nearly symmetric asteroids. Beyond this dependence on K_{2m} , almost no moment uncertainty variation is visible, indicating that this methodology will give similar results given many asteroid shapes distinct from the reference asteroid.

4.2 Comparison of Jupiter and Earth encounters

If sufficiently accurate spin pole data can be detected for non-Earth encounters, it may be possible to extract density moments for encounters with larger planets. In this section, we run our reference asteroid through a Jupiter encounter to analyze the differences in uncertainty.

The physical parameters of the asteroid body are kept the same as the Earth encounter case (listed in appendix B),

$K_{\ell m}$	$\sigma(K_{\ell m})_{\text{Jupiter}} / \sigma(K_{\ell m})_{\text{Earth}}$
γ_0	1.6
K_{22}	2.3
K_{20}	11
$\Re K_{33}$	18
$\Im K_{33}$	18
$\Re K_{32}$	18
$\Im K_{32}$	18
$\Re K_{31}$	25
$\Im K_{31}$	10
K_{30}	53

Table 2. Ratio of posterior uncertainty for all density moments $K_{\ell m}$ between an Earth encounter and a Jupiter encounter with identical properties except for an increased perigee. Observational uncertainty and cadence are assumed to be equivalent for the Jupiter and Earth encounters. Without taking the frequencies of close encounters into account, massive planets such as Jupiter yield less precise density moment estimates.

as are the observational uncertainty and cadence. The orbit is adjusted for the Jupiter case by setting a perijove distance of $r_p = 5$ Jupiter radii (compared to perigee radius $r_p = 5$ Earth radii for the Earth encounter). The excess velocity does not strongly affect $\sigma(K_{\ell m})$ as shown in section E1, so we keep it at the reference value. The ratio between the posterior uncertainties in the Jupiter and the Earth encounters are shown in table 2. In all cases, the Jupiter posteriors are more uncertain than Earth posteriors.

These uncertainty ratios can be understood as follows. The leading order of tidal torque is proportional to μ_A/D^3 . If D/a_B (the ratio of the encounter distance to the central body radius) is roughly constant (as in this case, where $r_p/a_B = 5$), then $\mu_A/D^3 \propto \rho_B$ where ρ_B is the density of the central body. Therefore, little advantage is to be gained by looking for encounters of a massive planet in this sense. Since Jupiter is less dense than Earth, we expect that un-

certainty in the first-order parameters γ_0 and K_{2m} would be slightly worse than in the case of Earth, which is seen in table 2.

The second-order terms are damped by an additional factor of a_A/D , which decreases if a massive central body is used. Since Jupiter is about 10 times larger in radius than Earth, we expect that the K_{3m} terms are about ten times more uncertain than the K_{2m} components, which is the case.

The $K_{\ell 0}$ components differ in that the posterior uncertainty increase for a Jupiter encounter over an Earth encounter is about five times greater for $K_{\ell 0}$ than other moments of the same ℓ . In fact, K_{30} essentially fills the prior. In section E6, we noted that $K_{\ell 0}$ is particularly uncertain when the asteroid does not tumble after the perigee. In this case, the Jupiter encounter resulted in less tumbling than the Earth encounter, so the larger increase in uncertainty in $K_{\ell 0}$ shown in table 2 is expected.

There are additional effects of central body mass which are not captured in this analysis. For example, encounters with massive planets are more plentiful, so that observation for a fixed period of time will lead to a larger number of observed encounters conducive to low-uncertainty moment extraction (large a_A , small r_p , etc.). The distribution of r_p in this encounter sample will also change; the ratio of the orbit impact parameter (the distance between the orbit asymptotes and the central body) to perijove distance is

$$\frac{b}{r_p} = \sqrt{1 + 2 \frac{G\mu_B}{r_p v_\infty^2}}. \quad (12)$$

It was mentioned above that the observable perigee distance r_p increases with $a_B \sim \mu_B^{1/3}$, so that $\frac{b}{r_p}$ is larger for more massive planets and therefore the same impact parameter leads to lower perijove. Other effects, such as a change in the physical properties of the encountering asteroids or decreased observational uncertainty due to the distance between Jupiter and Earth-based telescopes, may also affect the fit uncertainties. Which of these contradicting effects dominates is not immediately clear, and depends on the asteroid population near Jupiter and the observation method.

4.3 Finite element model DOF

The number of elements N used for the finite element model can be freely chosen. As discussed in section ??, seven of these are fixed by various constraints on the asteroid density distribution. There are 16 density moments with $\ell \leq 3$, so $N = 16$ with nine DOF is the largest number of parameters the model can support. However, maximizing the DOF adds model-induced uncertainty to our results. This uncertainty can be reduced by reducing N , but with $N < 16$, a solution perfectly matching the extracted moments is not guaranteed. There is therefore a trade-off between the average density uncertainty σ_ρ and the accuracy, which can be represented as the deviation of the density distribution from the true distribution $\Delta\rho$.

We investigate this trade-off by extracting five density distributions with five different finite-element layouts from moments extracted from synthetic data of the asymmetric reference asteroid. For each point in the asteroid, 1000 samples are drawn from each of the five density distributions. We use the standard deviation of the 5000 samples as the

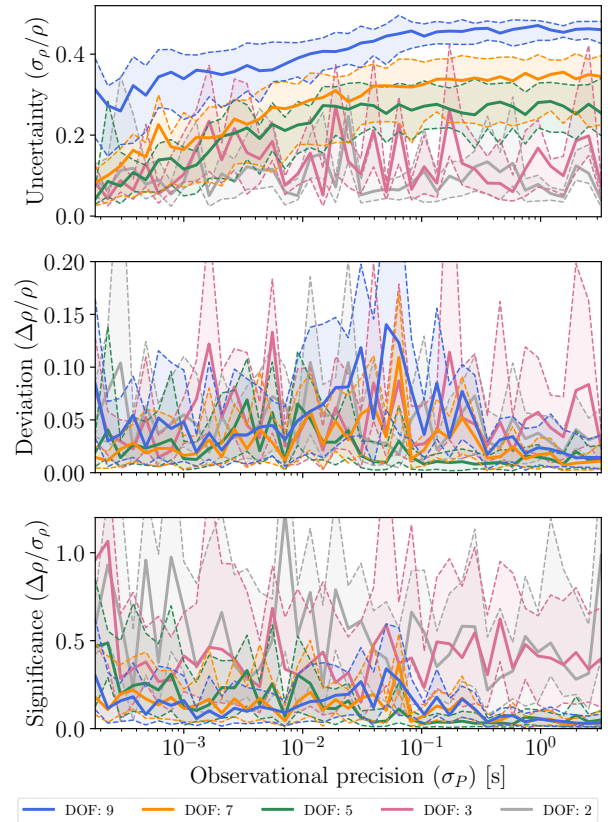


Figure 11. The average uncertainty σ_ρ and deviation from the truth $\Delta\rho$ of density distributions extracted by the finite element model with varying degrees of freedom. 5 DOF appears to optimize the trade-off between the model-induced uncertainty caused by too many DOF and the inaccuracy caused by too few.

uncertainty σ_ρ at that point, and the mean of the samples as the density ρ . Modelling the asteroid as having a uniform true density, we compute the deviation of the density from the truth $\Delta\rho$ over the asteroid. We do this for 9 (maximal), 7, 5, 3, and 2 DOF. Additionally, we vary the precision σ_P of the data set used to extract the density moments, and plot σ_ρ and $\Delta\rho$ as a function of σ_P . Figure 11 displays the distribution of σ_ρ , $\Delta\rho$, and the significance of the deviations from the truth ($\Delta\rho/\sigma_\rho$) over the asteroid.

The figure demonstrates the expected behaviour that few degrees of freedom result in low uncertainty but large $\Delta\rho/\sigma$, while many degrees of freedom is more accurate but also more uncertain. The trend of uncertainty, deviation, and significance as a function of σ_P is also discontinuous for few DOF, because in these cases the properties of the output distribution are strongly dependent on the initial choice of uncertainty of the initial choice of grids, and more than five grids are necessary to remove that dependence. This discontinuity is most noticeable for 3 and 2 DOFs, which also produce deviations from the true density distribution of the highest significance. We use 5 DOFs throughout this paper, produce the most precise results while still accurately reproducing the asteroid density distribution. 5 DOFs corresponds to $N = 12$ finite elements.

The top panel of 11 also demonstrates that σ_ρ reaches a plateau for large σ_P . In that regime, the prior constraints

that the density of the asteroid take on physically meaningful values are more constraining than the actual data, leading to less dependence on the data quality. This is a further example of how the extracted asteroid density distribution is strongly dependent on the choice of model, and one of the reasons why we display the uncertainties of density moments in section 4.1 rather than density distribution uncertainty. This moment uncertainty is not prone to the same model-dependent plateau.

4.4 Comparisons between density distribution models

In section 3.2, we displayed uniform and non-uniform density distributions extracted via the finite element and single-lump lumpy model. Here we highlight the success of the model in two other scenarios.

Figure 12 shows density distributions extracted via the finite element model and the lumpy model for an off-center core. Results are similar to the centred core shown in 5 in that the moments of the resulting density distribution are consistent with those extracted from the encounter data (i.e., χ_r^2 is low). Again, the finite element model does not isolate the lump, instead spreading the excess mass over the right side of the asteroid. The ability of the lumpy model to isolate the core is rooted in the fact that the shape of the asteroid is offset from the center of mass by a fixed amount with no uncertainty attached. The position of the lump is therefore set to balance the offset of the surrounding asteroid medium; the only free parameter is the lump’s mass, which determines this offset. The assumption that the asteroid’s center of mass is precisely known is rooted stems from the fact that the shape of the asteroid is observed to rotate around its center of mass. If observations do not allow the center of mass to be determined in this way, then the lump’s position will be more uncertain.

To assess the lumpy model when the positions of the lump are not as certain as in this off-center case, we consider an asteroid with two lumps of radius 300 m and density three times the surrounding density. Each lump is located 500 meters from the center of the asteroid, so that they counterbalance and the asteroid’s observed center of mass is its surface’s centroid. The lumpy model with $N = 2$ lumps then inherits three additional DOF corresponding to one lump’s position (the other lump is fixed to counterbalance it) as well as two more from the additional lump’s radius and mass. The model thus has seven DOF, in contrast to the 5 DOF of the finite element model. Both models are run on this asteroid and the resulting distributions are shown in figure 13.

Figure 13 again shows that the finite element model is unable to isolate the lumps except to predict generally increased asteroid near the center. On the other hand, the lumpy model detects that the two lumps are opposite each other, and of roughly the same radius and mass. These radius and mass values are also close to the true values. The model places the lumps correctly in the xy -plane of the asteroid but does not perfectly align them with the y axis, resulting in very high $\Delta\rho$ where the true lumps and predicted lumps do not intersect. Note that χ_r^2 remains low despite the lumpy model’s misplacement of the lumps. This is because the lumpy model gains its information on the placement of

the lumps from the K_{3m} density moments, which figures 8 and 9 suggest are not as well constrained as the K_{2m} density moments. The moments estimated by the MCMC fit to encounter data are not perfectly correct, resulting in a deviation of a few hundred meters in lump location. Overall, the figures show that even the poorly constrained K_{3m} moments can be used to determine features of the asteroid density, given a well-chosen model.

5 CONCLUSIONS

We derived a novel, arbitrary-order equation for the tidal torque experienced by an asteroid during an encounter with a planet of arbitrary shape and mass distribution. The tidal torque (equation 4) revealed that the angular velocity of the asteroid over time depends strongly on the asteroid’s density moments and the initial orientation. We then built a fast simulation for an asteroid encounter and designed an MCMC to extract density moments from simulated data. We also created two models — the finite element model and the lumpy model — to translate these density moments back into density distributions. Since this problem is underdetermined, the models give different results and were contrasted. Nevertheless, we find that the models always produce results consistent with the data set. The entire pipeline was run starting from simulated encounter data and ending with density distribution predictions and was shown to be robust.

We assessed the uncertainty of the pipeline’s results by adjusting various properties of the asteroid and its Earth encounter. The precise thresholds we measure (table 1) show that the observational uncertainty and perigee of the asteroid orbit have the strongest effect on the density distribution uncertainty and they are the most important thresholds to meet in order to extract a precise distribution. We also discussed how these thresholds could be eased by changes in observational behaviour such as lengthening the data set, or by physical asteroid properties such as a closer encounter or an initially tumbling state. If the thresholds were eased enough, then the asteroid length would become an important threshold as well.

Finally, we highlighted that the properties of the final density distribution are strongly dependent. The uncertainties on density distribution of the two models were drastically different, and also depended on the number of degrees of freedom used in the model. For asteroids of non-uniform distributions, the distributions themselves also differed. The lumpy model, designed to look for specific types of features, was much more sensitive to these features than the generic finite element model. To efficiently use encounter data, it is therefore important to investigate multiple models and choose different models to answer different questions.

ACKNOWLEDGEMENTS

We warmly thank Emmanuel Jehin, Maxime Devogele, and Marin Ferrais for meeting with the authors to discuss this work and pointing out possible future initiatives. JTD also thanks the MIT UROP office for funding his work. This paper made substantial use of MIT Supercloud’s facilities.

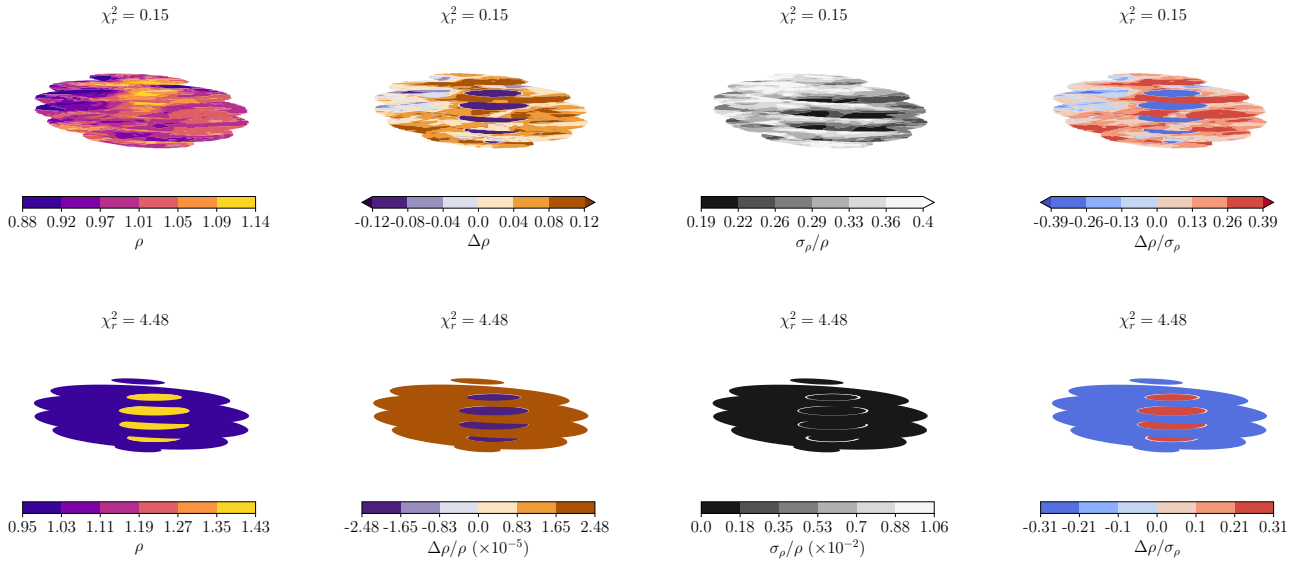


Figure 12. Cross-sectional slices of the density distributions extracted via the finite-element (*top*) and lumpy (*bottom*) models for an asteroid with an off-center core. From left to right, the densities, deviations from the true density, uncertainties, and significance of the deviations are plotted. These figures are available in animated form in appendix figure F3. The core is successfully extracted in all cases.

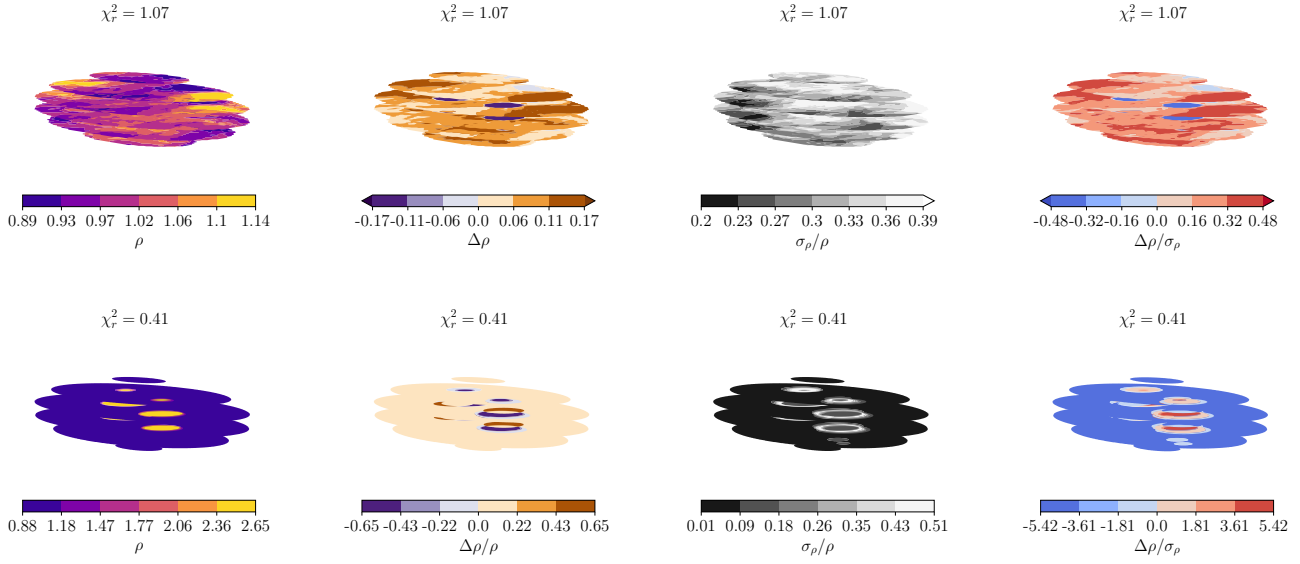


Figure 13. Cross-sectional slices of the density distributions extracted via the finite-element (*top*) and the two-lump lumpy (*bottom*) models for an asteroid with two counterbalancing cores. From left to right, the densities, deviations from the true density, uncertainties, and significance of the deviations are plotted. These figures are available in animated form in appendix figure F4. The additional lump greatly increases uncertainty, but the resulting distribution is close to accurate.

DATA AVAILABILITY

The asteroid simulation, fit process, and density moment extraction code are available on [GitHub](#). Please contact JTD with questions.

REFERENCES

- Ashenberg J., 2007, *Celestial Mechanics and Dynamical Astronomy*, 99, 149
- Benson C. J., Scheeres D. J., Moskovitz N. A., 2020, *Icarus*, 340, 113518
- Berthier J., et al., 2020, *Icarus*, 352, 113990
- Boué G., Laskar J., 2009, *Icarus*, 201, 750
- Brown T., et al., 2013, *Publications of the Astronomical Society of the Pacific*, 125, 1031

- Carroll K., Faber D., 2018, in Proceedings of the 69th International Astronautical Congress.
- Descamps P., et al., 2020, *Icarus*, 345, 113726
- Devogèle M., et al., 2021, *Monthly Notices of the Royal Astronomical Society*, 505, 245
- Foreman-Mackey D., Hogg D. W., Lang D., Goodman J., 2013, *Publications of the Astronomical Society of the Pacific*, 125, 306
- Gao F., Han L., 2012, *Computational Optimization and Applications*, 51, 259
- Giorgini J., Benner L., Nolan M., Ostro S., 2005, in AAS/Division of Dynamical Astronomy Meeting# 36. pp 02–01
- Giorgini J. D., Benner L. A., Ostro S. J., Nolan M. C., Busch M. W., 2008, *Icarus*, 193, 1
- Hirabayashi M., Kim Y., Brozović M., 2021, *Icarus*, 365, 114493
- Hou X., Scheeres D. J., Xin X., Mar 2017, *Celestial Mechanics and Dynamical Astronomy*, 127, 369
- Kaasalainen M., 2001, *Astronomy & Astrophysics*, 376, 302
- Kaiser N., et al., 2002, in *Survey and Other Telescope Technologies and Discoveries*. pp 154–164
- Larson S., Brownlee J., Hergenrother C., Spahr T., 1998, in *Bulletin of the American Astronomical Society*. p. 1037
- Lee H.-J., et al., 2022.
- Makarov V. V., Goldin A., Tkachenko A. V., Veras D., Noyelles B., 2022.
- Moskovitz N. A., et al., 2020, *Icarus*, 340, 113519
- Naidu S. P., Margot J.-L., 2015, *The Astronomical Journal*, 149, 80
- Pater D. I., Lissauer J. J., 2015, *Planetary sciences*, 2 edn. Cambridge University Press
- Paul M. K., 1988, *Celestial mechanics*, 44, 49
- Pravec P., et al., 2014, *Icarus*, 233, 48
- Richardson D. C., Bottke W. F., Love S. G., 1998, *Icarus*, 134, 47
- Richardson J. E., Melosh H. J., Greenberg R. J., O'Brien D. P., 2005, *Icarus*, 179, 325
- Scheeres D., Ostro S., Werner R., Asphaug E., Hudson R., 2000, *Icarus*, 147, 106
- Scheeres D. J., Marzari F., Rossi A., 2004, *Icarus*, 170, 312
- Smalley K., Garradd G., Benner L., Nolan M., Giorgini J., Chesley S., Ostro S., Scheeres D., 2005, *International Astronomical Union Circular*, 8477, 1
- Souchay J., Souami D., Lhotka C., Puente V., Folgueira M., 2014, *Astronomy & Astrophysics*, 563, A24
- Souchay J., Lhotka C., Heron G., Herve Y., Puente V., Lopez M. F., 2018, *Astronomy & Astrophysics*, 617, A74
- Stokes G. H., Evans J. B., Viggh H. E., Shelly F. C., Pearce E. C., 2000, *Icarus*, 148, 21
- Tyson J. A., 2002, *Survey and Other Telescope Technologies and Discoveries*, 4836, 10
- Valvano G., Winter O. C., Sfair R., Machado Oliveira R., Borderes-Motta G., Moura T., 2022, *Monthly Notices of the Royal Astronomical Society*, 510, 95
- Wright E. L., et al., 2010, *The Astronomical Journal*, 140, 1868
- Yu Y., Richardson D. C., Michel P., Schwartz S. R., Ballouz R.-L., 2014, *Icarus*, 242, 82
- van Gelderen M., 1998, in *The shift operators and translations of spherical harmonics*.

APPENDIX A: TIDAL TORQUE & EQUATIONS OF MOTION

In this appendix, we derive the equations of motion used to simulate the asteroid angular velocity during the encounter. In particular, we describe our coordinates (section A1) for an encountering asteroid's position and orientation,

and we parametrize its density distribution via its “density moments” (section A2). Then we derive an arbitrary-order equation for tidal torque (section A3) and write the equations of motion for the system (section A4). We do not consider any third-body perturbations, and we assume that the body being encountered (the central body, e.g. a planet) is much more massive than the asteroid.

A1 Coordinates

We make use of two frames of reference to model this system. One is the “inertial frame,” with axes denoted by $\hat{\mathbf{X}}, \hat{\mathbf{Y}}, \hat{\mathbf{Z}}$ and origin placed at the central body's centre of mass. $\hat{\mathbf{X}}$ points from the central body to the asteroid periapse, and $\hat{\mathbf{Z}}$ points parallel to the orbit angular momentum. We assume that the mass distribution of the central body is known in this inertial frame.

Our second frame is the “body-fixed” frame, denoted by $\hat{\mathbf{x}}, \hat{\mathbf{y}}, \hat{\mathbf{z}}$. Each axis in this frame is aligned with a principal axis and rotates with the asteroid, with its origin at the asteroid's centre of mass. For definiteness, we define $\hat{\mathbf{z}}$ to be the principal axis with maximal moment of inertia (this is the short axis mode, to use the vocabulary of Ref. [Kaasalainen \(2001\)](#)). In general, we use capital letters to denote vectors in the inertial frame and lowercase vectors to denote vectors in the body-fixed frame.

The difference between the origins of the body-fixed and inertial frames is the position of the asteroid. We represent the relative orientations by $z - y - z$ Euler angles α, β , and γ , such that a matrix M rotating from the body-fixed to the inertial frame ($M\mathbf{r} = \mathbf{R}$) is given by

$$M = R_z(\alpha)R_y(\beta)R_z(\gamma). \quad (\text{A1})$$

Here, $R_i(\theta)$ is a rotation around the unit vector i by θ (figure A1).

A2 Density moments

In the next section, it will be shown that only certain parameters of the asteroid density distribution affect tidal torque called “density moments.” First, we define the unnormalized spherical harmonics $Y_{\ell m}(\theta, \phi) = P_{\ell m}(\cos \theta)e^{im\phi}$, where $P_{\ell m}$ are the associated Legendre Polynomials without the Condon-Shortley phase. The regular and irregular spherical harmonics then defined as

$$\begin{aligned} S_{\ell m}(\mathbf{r}) &= (-1)^m (\ell - m)! \frac{Y_{\ell m}(\hat{\mathbf{r}})}{r^{\ell+1}} \\ R_{\ell m}(\mathbf{r}) &= (-1)^m \frac{r^\ell}{(\ell + m)!} Y_{\ell m}(\hat{\mathbf{r}}). \end{aligned} \quad (\text{A2})$$

These spherical harmonics obey many useful identities summarized in Ref. [van Gelderen \(1998\)](#), which are also useful for quantum mechanics. They were used to define the density moments in equation 1, which can be extended to the central body:

$$J_{\ell m} = \frac{a_{\mathcal{B}}^{2-\ell}}{I_{\mathcal{B}}} \int_{\mathcal{B}} d^3 r \rho_{\mathcal{B}}(\mathbf{r}) R_{\ell m}(\mathbf{r}) \quad (\text{A3})$$

By contrast, $J_{\ell m}$ should be computed in the inertial frame. The length scale $a_{\mathcal{B}}$ and MOI scale $I_{\mathcal{B}}$ can be defined similarly to $a_{\mathcal{A}}$ and $I_{\mathcal{B}}$ in equations 3 and 2, but they could also

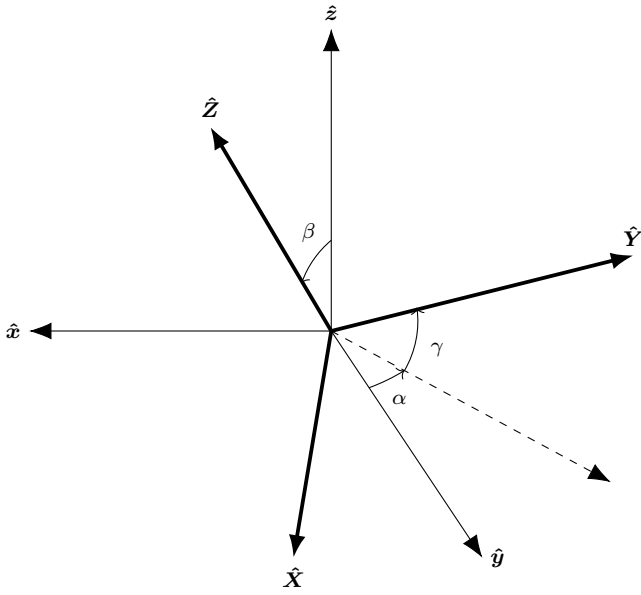


Figure A1. $z - y - z$ Euler angles used in this work to express the orientation of the asteroid. Orientation is expressed as a rotation from the body-fixed axes (lowercase) to the inertial axes (bold and uppercase). The origins are co-located for demonstration purposes.

be set to any other scales of the proper units, e.g. a_B equal to the central body radius and $I_B = \mu_B a_B^2$, where μ_B is the central body mass.

Note that both $J_{\ell m}$ and $K_{\ell m}$ are unitless. We call them “moments” because the $R_{\ell m}(\mathbf{r})$ contains an r^ℓ dependence so that $K_{\ell m}$ is the ℓ th density moment of the asteroid. The gravitational potential field of the asteroid can be written entirely in terms of $K_{\ell m}$ and a_A , so we expect not to need any information about the density distribution of the asteroid beyond these parameters to compute tidal torque.

These moments share several key properties which we discuss before continuing. Firstly, for real mass density, properties of the spherical harmonics imply that $K_{\ell m} = (-1)^m K_{\ell, -m}^*$. Therefore, the set of $K_{\ell m}$ for $\ell < \ell_{\max}$ contains ℓ_{\max}^2 degrees of freedom. However, some of these degrees of freedom are redundant with the choice of coordinates: $K_{1m} = 0$ since the body-fixed frame is centred on the asteroid centre of mass. Further calculation reveals that the alignment of the body-fixed frame with the asteroid principal axes also forces $K_{21} = 0$ and $\Im K_{22} = 0$. The only physical density moments for $\ell \leq 2$ are therefore K_{22} , K_{20} , and K_{00} . The first two are related to the moment of inertia around each principal axis by equation 5, while $K_{00} = \mu_A a_A^2 / I_A$ will not be relevant to this study as it does not appear in 4.

The physical meaning of K_{22} and K_{20} can also be interpreted via a special case: if the asteroid is a uniform-density triaxial ellipsoid, the moments of inertia are simple to compute in terms of the semi-axis lengths and can be compared to those found in equation 5. This yields semi-axis lengths

ℓ	$\Re K_{\ell 3}$	$\Im K_{\ell 3}$	$\Re K_{\ell 2}$	$\Im K_{\ell 2}$	$\Re K_{\ell 1}$	$\Im K_{\ell 1}$	$K_{\ell 0}$
0							-
1					x	y	z
2			-	x,y	y,z	x,z	-
3	x,z	y,z	z	x,y,z	x	y	z

Table A1. Axes of mirror symmetry that imply zeroed density moments. For example, for mirror symmetries along \hat{y} or \hat{z} , $\Im K_{32} = 0$. Mirror symmetry along \hat{x} means $\rho_A(x, y, z) = \rho_A(-x, y, z)$. Dashes indicate that none of the mirror symmetries zero the moment in question. Since $r^2 > 0$ for $r \neq 0$, no symmetries set $a_A = 0$ either.

of

$$\begin{aligned} a &= \sqrt{\frac{5}{3}} a_A \sqrt{1 - 2K_{20} + 12K_{22}} \\ b &= \sqrt{\frac{5}{3}} a_A \sqrt{1 - 2K_{20} - 12K_{22}} \\ c &= \sqrt{\frac{5}{3}} a_A \sqrt{1 + 4K_{20}}. \end{aligned} \quad (\text{A4})$$

The higher-order moments K_{3m} can be thought of loosely as measuring the large-scale asymmetries of the asteroid. An asteroid that is mirror-symmetric along the \hat{x} axis (meaning $\rho_A(x, y, z) = \rho_A(-x, y, z)$) necessarily sets certain density moments to zero. Which density moments are zeroed by which mirror symmetries is outlined in table A1. All K_{3m} are zeroed by at least one mirror symmetry.

Finally, the requirement that $\rho_A(\mathbf{r}) \geq 0$ everywhere restricts $K_{\ell m}$. In the case of K_{2m} , this fact and the constraint that I_z is larger than I_x or I_y requires K_{20} and K_{22} to fall in the triangle

$$-\frac{1}{4} \leq K_{20} \leq 0, \quad |K_{22}| \leq -\frac{K_{20}}{2}. \quad (\text{A5})$$

An analytical constraint on K_{3m} based on this property is more difficult to derive, but in practice, we also observe that $|K_{3m}| < 0.01$.

A3 Tidal torque

Derivations for the tidal torque experienced by a rigid body in the gravitational field of a larger mass have been computed by several previous studies Paul (1988); Hou et al. (2017); Boué & Laskar (2009); Ashenberg (2007), often in terms of the moment of inertia of the rigid body (or higher order moments of inertia), and to varying degrees of precision. A simple, first-order derivation is also easily computable in terms of the asteroid moment of inertia in the inertial frame.

Here, we present a new derivation of the tidal torque to arbitrary orders in terms of the density moments of an asteroid defined in section A2. These density moments can be pre-computed and do not have to be re-evaluated every time-step.

Throughout this paper, we assume that the asteroid remains rigid throughout the encounter. We also assume no third-body perturbations from other Solar System objects. (More accurately, we assume that all third-body perturbing objects lie closer to the central body’s centre of mass than the asteroid perigee distance so that their density moments can be included in the density moments of the central body.) For the sake of simplicity, we also assume that the density

moments of the central body are known and do not evolve with time (i.e., the central body's rotation is marginal compared to the timescale of the encounter).

The gravitational potential energy of the central body is, in its most general form,

$$V(\mathbf{R}') = -G \int_{\mathcal{B}} d^3 R \rho_{\mathcal{B}}(\mathbf{R}) \frac{1}{|\mathbf{R} - \mathbf{R}'|}. \quad (\text{A6})$$

where $\rho_{\mathcal{B}}$ is the density distribution of the central body and \mathcal{B} indicates the central body's volume. All vectors here are written in the inertial frame. Given $|\mathbf{R}| < |\mathbf{R}'|$, Ref. van Gelderen (1998) gives the identity

$$\frac{1}{|\mathbf{R} - \mathbf{R}'|} = \sum_{\ell, m} R_{\ell m}(\mathbf{R}) S_{\ell m}^*(\mathbf{R}'), \quad (\text{A7})$$

where the sum is shorthand for $\sum_{\ell, m} = \sum_{\ell=0}^{\infty} \sum_{m=-\ell}^{\ell}$. We are interested in translating the potential energy of equation A6 to the body-fixed frame. To do this, we let $\mathbf{R}' = \mathbf{D} + \mathbf{U}$, where \mathbf{D} is the location of the asteroid in the inertial frame. We further define $\mathbf{U} = M\mathbf{u}$, where \mathbf{u} is in the body-fixed frame and M is the rotation matrix given by the Euler angles α, β , and γ (see section A1). The translation from \mathbf{R}' to \mathbf{U} is then attained by the identity

$$S_{\ell m}(\mathbf{R}') = \sum_{\ell', m'} (-1)^{\ell'} R_{\ell' m'}^*(\mathbf{U}) S_{\ell + \ell', m + m'}(\mathbf{D}), \quad (\text{A8})$$

provided by Ref. van Gelderen (1998), and from \mathbf{U} to \mathbf{u} is given by

$$Y_{\ell m}(M\mathbf{u}) = \sum_{m'=-\ell}^{\ell} (-1)^{m+m'} \sqrt{\frac{(\ell-m')!(\ell+m)!}{(\ell+m')!(\ell-m)!}} \times \mathcal{D}_{mm'}^{\ell}(M)^* Y_{\ell m'}(\mathbf{u}). \quad (\text{A9})$$

Here, $\mathcal{D}_{mm'}^{\ell}(M)$ are the Wigner-D matrices, which are determined by the Euler angles α, β , and γ of M .

Equations A6 to A9 then provide formula for $V(\mathbf{u})$ expressed as a sum of integrals over \mathcal{B} of the central body density $\rho_{\mathcal{B}}(\mathbf{R})$ times $R_{\ell m}(\mathbf{R})$. These are expressed via equation A3 as $J_{\ell m}$.

The tidal torque experienced by the asteroid (in the body-fixed frame) is given by

$$\boldsymbol{\tau}(\mathbf{u}) = \int_{\mathcal{A}} d^3 u \rho_{\mathcal{A}}(\mathbf{u}) (\mathbf{u} \times (-\nabla_{\mathbf{u}} V(\mathbf{u}))) \quad (\text{A10})$$

where $\rho_{\mathcal{A}}$ is the density distribution of the asteroid and \mathcal{A} indicates the volume of the asteroid. Making use of one more identity concerning the derivatives of spherical harmonics:

$$\begin{aligned} \mathbf{u} \times \nabla R_{\ell m}(\mathbf{u}) = & \frac{1}{2} [(i\hat{x} - \hat{y})(\ell - m + 1) R_{\ell, m-1}(\mathbf{u}) \\ & + (i\hat{x} + \hat{y})(\ell + m + 1) R_{\ell, m+1}(\mathbf{u}) \\ & + 2im\hat{z} R_{\ell m}(\mathbf{u})], \end{aligned} \quad (\text{A11})$$

tidal torque can now be expressed as a function only of the constants $J_{\ell m}$, $K_{\ell m}$, $a_{\mathcal{A}/\mathcal{B}}$, $I_{\mathcal{A}/\mathcal{B}}$, and the asteroid orientation and position (equation 4). Some $K_{\ell m}$ terms are written in this equation with $|m| > \ell$; these should all be taken to be zero.

Equation 4 possesses a few explicit properties. Firstly, $\boldsymbol{\tau}$ is independent of asteroid mass. The mean density of the asteroid is therefore not constrained by tidal torque analysis. Secondly, torque is largest when D is small (as expected),

with the leading order of $\boldsymbol{\tau}$ proportional to D^{-3} . Thirdly, each $J_{\ell m} K_{\ell' m'}$ term is multiplied by $(a_{\mathcal{B}}/D)^{\ell} (a_{\mathcal{A}}/D)^{\ell'}$, the latter of which especially is small in most cases. Equation 4 can therefore be computed approximately by removing terms of large ℓ and ℓ' . For our analysis, we removed $\ell' > 3$ and we usually keep only $\ell = 0$. Note that $\ell = 1$ contributes nothing since $J_{1m} = 0$. J_{2m} measures the oblateness and its effects are studied in appendix E.

Further insight can be gained by remarking the value of the first-order of $\boldsymbol{\tau}$ for particular Euler angle cases. Setting $\beta = 0$ produces diagonal Wigner-D matrices, and hence $\boldsymbol{\tau} \parallel \hat{z}$ to first-order. Also, the component τ_z oscillates, so that for certain values of α and γ , $\boldsymbol{\tau} = 0$. This $\beta = 0$ condition is equivalent to $\hat{z} \parallel \hat{Z}$ (see figure A1).

For $\beta = \pi/2$, there are two interesting cases. One is for $\alpha = \phi$ (or $\alpha = \pi + \phi$), where ϕ is the angle between the asteroid and the perigee. In this case, $\boldsymbol{\tau} = 0$ to first-order. The second case is $\alpha = \phi \pm \pi/2$, when again $\boldsymbol{\tau} \parallel \hat{z}$ and τ_z oscillates. At perigee ($\phi = 0$), these conditions are equivalent to $\hat{z} \parallel \hat{X}$ and $\hat{z} \parallel \hat{Y}$ respectively.

The $\boldsymbol{\tau} \parallel \hat{z}$ cases are interesting because they do not induce tumbling. If velocity is $\boldsymbol{\omega} \parallel \hat{z}$ (a non-tumbling state, since \hat{z} is a principal axis), then $\boldsymbol{\omega} \parallel \mathbf{L}$ and $\boldsymbol{\tau} = \dot{\mathbf{L}} \parallel \dot{\boldsymbol{\omega}}$ so that $\boldsymbol{\omega}$ remains parallel to \hat{z} and non-tumbling. These cases of torque are additionally significant because not as many terms contribute to τ_z as to τ_x and τ_y .

A4 Equations of motion

The equations of motion of the asteroid position \mathbf{D} are given by Newton's law of gravitation

$$\dot{\mathbf{V}} = -\frac{G\mu_{\mathcal{B}}}{D^3} \mathbf{D} \quad \dot{\mathbf{D}} = \mathbf{V} \quad (\text{A12})$$

where \mathbf{V} is the asteroid velocity in the inertial frame. Rather than derive equations of motion for the Euler angles (which suffer from gimbal lock), we instead represent the orientation of the asteroid with a quaternion $\tilde{\mathbf{q}}$ which can be converted into Euler angles to compute $\mathcal{D}(\alpha, \beta, \gamma)$. This quaternion evolves as

$$\dot{\tilde{\mathbf{q}}} = \frac{1}{2} \tilde{\mathbf{q}} \tilde{\boldsymbol{\omega}}. \quad (\text{A13})$$

for angular velocity $\boldsymbol{\omega}$ given in the body-fixed frame. The equations of motion of $\boldsymbol{\omega}$ in turn are given by

$$\begin{aligned} I_x \dot{\omega}_1 - \omega_y \omega_z (I_y - I_z) &= \tau_x \\ I_y \dot{\omega}_2 - \omega_z \omega_x (I_z - I_x) &= \tau_y \\ I_z \dot{\omega}_3 - \omega_x \omega_y (I_x - I_y) &= \tau_z. \end{aligned} \quad (\text{A14})$$

Equations 4, 5, and A12 to A14 form a set of non-linear, first-order coupled differential equations in which can be numerically integrated. They are expressed in terms of the constant physical parameters $I_{\mathcal{A}/\mathcal{B}}$, $a_{\mathcal{A}/\mathcal{B}}$, $J_{\ell m}$, and $K_{\ell m}$.

Note that equation A14 is independent of $a_{\mathcal{A}}$ to first-order in $\boldsymbol{\tau}$, because $I_j \propto a_{\mathcal{A}}^2$ for all j and $\boldsymbol{\tau} \propto a_{\mathcal{A}}^2$. Therefore, scaling $a_{\mathcal{A}}$ merely scales the value of the sub-leading-order contributions to $\boldsymbol{\tau}$.

APPENDIX B: REFERENCE ASTEROID CONFIGURATIONS

Except when otherwise mentioned, we use the following asteroid encounter parameters. Many of the parameter choices are made to maximize the quality of observations (a close orbit, large asteroid, etc.) This is so that our analysis is most sensitive to the affect changing these parameters to the methodology's output.

- (i) An orbit around a spherical, Moonless Earth with 6 km s^{-1} excess velocity and perigee at 5 Earth radii. This orbit was chosen to roughly match that of 99942 Apophis [Giorgini et al. \(2005, 2008\)](#); [Smalley et al. \(2005\)](#), discovered on June 19, 2004 by R. A. Tucker, D. J. Tholen, and F. Bernardi. These orbital parameters correspond to an eccentricity of 3.88. The comparison to Apophis is complicated by the fact that Apophis is smaller than our $a_{\mathcal{A}}$ value, is tumbling [Pravec et al. \(2014\)](#), and may change slightly in physical properties due to tidal interaction during the encounter [Yu et al. \(2014\)](#); [Hirabayashi et al. \(2021\)](#). Further work must therefore be done to apply this analysis to Apophis.
- (ii) An initial roll of $\gamma_0 = \pi/8$.
- (iii) A cadence of 2 minutes and observational uncertainty of $\sigma_{\theta} = 0.01$ and $\sigma_P/P = 10^{-7}$.
- (iv) A rotational period of 9 hours, with the angular velocity vector distributed between the $\hat{\mathbf{X}}$, $\hat{\mathbf{Y}}$, and $\hat{\mathbf{Z}}$ axes in a $1 : 2 : -2$ ratio.

(v) An asteroid with radius $a_{\mathcal{A}} = 1 \text{ km}$ and $K_{3m} = 0$. For K_{22} and K_{20} , we use two standard values: one with $(K_{22}, K_{20}) = (0, -0.097)$ and one with $(0.052, -0.202)$. Including the third point obtained by reflection $K_{22} \rightarrow -K_{22}$, these are the three points that minimize the mean distance between an arbitrary point in the allowed parameter space (equation A5) and these reference values. The first point is called the symmetric case because the corresponding uniform-density-ellipsoid model is rotationally symmetric around $\hat{\mathbf{z}}$. The second case and its reflection are called the asymmetric cases. Values of $(0.052, -0.202)$ have $a < b$ in the ellipsoid model, and the reflected value has $a > b$. If not specified, we use the $a < b$ case. Specifically, the asymmetric case has $a = 1140 \text{ m}$, $b = 1839 \text{ m}$, and $c = 565 \text{ m}$, while the symmetric case has $a = b = 1411 \text{ m}$ and $c = 1008 \text{ m}$.

The surface of a spherical asteroid with this rotational period and $a_{\mathcal{A}}$ rotates at 25 cm s^{-1} at the equator. The asymmetric and symmetric ellipsoids have maximum equatorial velocities of 36 cm s^{-1} and 27 cm s^{-1} respectively.

APPENDIX C: ADDITIONAL DENSITY DISTRIBUTION MODELS

Two models were discussed in section 2.4 to translate density moment constraints into density distribution constraints. Here we outline two additional models, the nearly-uniform and the harmonic models, which are less conventional but still useable for extracting density distribution properties. Unlike the finite element and lumpy models discussed in the main text, these models will yield smooth distributions with no discrete transitions. They also rely on a known surface for the asteroid.

C1 Nearly-uniform model

In this nearly-uniform model, we seek to pick one density distribution from the many distributions consistent with the data by maximizing a prior distribution $f[\rho(\mathbf{r})]$, which can be chosen manually. Any prior distribution can be chosen, but the following prior is both interesting and numerically efficient.

As part of our prior, we require that the asteroid density distribution satisfy $I_{\mathcal{A}} = \mu_{\mathcal{A}} a_{\mathcal{A}}^2$. This constraint is desirable as it encourages nearly uniform density distributions; recall that a perfectly uniform asteroid always satisfies this constraint. To define the prior, we divide the asteroid into $n \gg 1$ small regions of volume V , each with position \mathbf{r}_i and density $\rho_i = \delta_i + 1$. Setting the mass of the asteroid equal to its volume, the average density is 1, so δ_i is the difference between the average and local density. We set $f[\rho(\mathbf{r})]$ to be a multivariate-Gaussian distribution on δ_i centred on zero to minimize non-uniformity, i.e.

$$f[\rho(\mathbf{r})] \propto \prod_i \exp\left(-\frac{\delta_i^2}{2\sigma^2}\right) \implies \ln f[\rho(\mathbf{r})] \simeq -\sum_i \delta_i^2 \quad (\text{C1})$$

where σ is an irrelevant constant. The density moments, MOI scale, and mass are

$$K_{\ell m} = \frac{V}{\mu_{\mathcal{A}} a_{\mathcal{A}}^{\ell}} \sum_i (\delta_i + 1) R_{\ell m}(\mathbf{r}_i) \quad (\text{C2})$$

$$I_{\mathcal{A}} = \mu_{\mathcal{A}} a_{\mathcal{A}}^2 = V \sum_i (\delta_i + 1) r_i^2 \quad (\text{C3})$$

$$\mu_{\mathcal{A}} = V \sum_i (\delta_i + 1) \implies 0 = \sum_i \delta_i. \quad (\text{C4})$$

Writing δ_i as an n -dimensional vector $\boldsymbol{\delta}$, equation C2 is a matrix equation for $K_{\ell m}$ and equations C3 and C4 are vector dot product equations. Combining $K_{\ell m}$, $I_{\mathcal{A}}$, and 0 into a single vector \mathbf{K} , these equations can be written as a single underdetermined matrix equation we denote as $\mathbf{K} = M\boldsymbol{\delta} + \mathbf{C}$, where the components of constant matrix M and constant vector \mathbf{C} are known given a fixed layout of the n regions. Some of the components of \mathbf{K} , such as $I_{\mathcal{A}}$, $\mu_{\mathcal{A}}$, and K_{1m} , are constraints. We treat the other components as parameters of the model. The task is then to find $\boldsymbol{\delta}$ that satisfies this matrix equation and maximizes $f(\boldsymbol{\delta})$. But the form of equation C1 shows that the maximum of $\ln f$ (and the maximum of f) is the minimum of $|\boldsymbol{\delta}|^2$. The value of $\boldsymbol{\delta}$ that obeys the constraints and minimizes its norm is given by the Moore-Penrose inverse:

$$\boldsymbol{\delta} = M^+ (\mathbf{K} - \mathbf{C}); \quad M^+ = M^\dagger (MM^\dagger)^{-1} \quad (\text{C5})$$

where M^\dagger is the adjoint of M .

The probability distribution of \mathbf{K} is given by the output of the fit described in section 2.3. The parameters of this model, \mathbf{K} , might differ from this distribution due to the additional constraint that the density fall in realistic values. This can be implemented by individually checking the components $\boldsymbol{\delta}$ computed by equation C5 and confirming that $1 + \delta_i$ lies within the acceptable range of densities.

C2 Harmonic model

For the harmonic model, we limit ourselves to density distributions that are harmonic; i.e., they satisfy $\nabla^2 \rho(\mathbf{r}) = 0$.

We have no physical justification for why this assumption should be true, but it is useful as a simplification to gain qualitative insight into the properties of the asteroid density distribution.

A harmonic density distribution can be expanded in terms of the spherical harmonics as $\rho(\mathbf{r}) = \sum_{\ell m} C_{\ell m} R_{\ell m}(\mathbf{r})^*$ where $C_{\ell m}$ are complex, free parameters. This series can be truncated at some maximum ℓ . The density moments, MOI scale, and mass can then be explicitly computed as a function of $C_{\ell m}$:

$$K_{\ell m} = \frac{a_{\mathcal{A}}^{2-\ell}}{I_{\mathcal{A}}} \sum_{\ell m} C_{\ell' m'} \int_{\mathcal{A}} d^3 r R_{\ell' m'}(\mathbf{r})^* R_{\ell m}(\mathbf{r}) \quad (\text{C6})$$

$$I_{\mathcal{A}} = \sum_{\ell m} C_{\ell m} \int_{\mathcal{A}} d^3 r R_{\ell m}(\mathbf{r})^* r^2 \quad (\text{C7})$$

$$\mu_{\mathcal{A}} = \sum_{\ell m} C_{\ell m} \int_{\mathcal{A}} d^3 r R_{\ell m}(\mathbf{r})^*. \quad (\text{C8})$$

These integrals can be pre-computed given a known asteroid shape \mathcal{A} , so that computing $C_{\ell m}$ to match a given $K_{\ell m}$ is fast. Furthermore, their values when \mathcal{A} is spherical gives us insight into the influence of $K_{\ell m}$ on density distributions. In this case, $I_{\mathcal{A}} \propto C_{00}$ and the integral of equation C6 is nonzero only when $\ell' = \ell$ and $m' = m$. Therefore, $C_{\ell m}$ is proportional to $K_{\ell m}$. The density distribution can be immediately visualized given the density moments as a sum of the solid spherical harmonics weighted by $K_{\ell m}$. When the asteroid is non-spherical, the shape itself contributes to $K_{\ell m}$ so as to break this picture.

Imposing constraints on these moments is also necessary. The choice of mass is enforced merely by enforcing equation C8. We impose bounds on $\rho(\mathbf{r})$ by acknowledging that harmonic functions such as $\rho(\mathbf{r})$ in a region such as \mathcal{A} attain their maxima on the boundary of the region, so that it is only necessary to ensure that ρ lies within the allowed range on the asteroid boundary rather than within the entire asteroid. This can be done by parametrizing the asteroid surface as a function of two variables and minimizing and maximizing ρ with respect to those variables, ensuring these minima and maxima are within the allowed range.

APPENDIX D: THE CADENCE CUT-OFF

JTD: Remove this section or included it in the following section.

In section E4, we noted that posterior uncertainty as a function of observation cadence Δt appears to increase suddenly near $\Delta t \sim T_{\text{cad}} = 30 - 40$ min. In this appendix, we discuss the location of this cadence cut-off as a function of the physical parameters of the asteroid.

In figure D1, we display contour plots of posterior uncertainty $\sigma(K_{\ell m})$ of the fit parameters as a function of both cadence Δt and P_{ω} (left panel) or the relative orbit speed $t_{\text{spin}}/t_{\text{orbit}}$ (right panel). Both panels show the same sudden increase in posterior uncertainty we named T_{cad} , located around the region where $\sigma_{\rho}/\rho = 100\%$ and now visible as a function of frequency and relative orbit speed. In all cases, the value of γ_0 was set so that all data points achieve the same value of γ at perigee.

Figure D1 demonstrates that large rotational period produces high T_{cad} . The dependence on P_{ω} agrees with the fact that large rotational periods for fixed cadence lead to better posterior uncertainty, discussed in section E7. The figure also demonstrates that for large P_{ω} , T_{cad} depends less strongly on P_{omega} and may even reverse its dependence such that increasing P_{omega} decreases T_{omega} . In all cases except $\mathcal{R}K_{33}$, at least constant- $\sigma(K_{\ell m})$ contour is seen to curve back such that Δt decreases as a function of P_{omega} for large P_{omega} . In these regions the cadence cut-off also dulls, as shown by the spreading of the constant- $\sigma(K_{\ell m})$ contours in this region.

The relative orbit speed $t_{\text{spin}}/t_{\text{orbit}}$ was defined by unphysically increasing or decreasing the time at which the asteroid moved through the orbit determined by the equations of motion (but leaving the orbit shape unchanged). The equations of motion affecting the orientation and spin of the asteroid however were unaffected. $t_{\text{spin}}/t_{\text{orbit}} > 1$ corresponds to a faster orbit, and $t_{\text{spin}}/t_{\text{orbit}} < 1$ corresponds to a slower orbit. With this unphysical process, we isolate the effect of the amount of time spent near perigee on posterior uncertainty, without inheriting additional affects that would have been caused by the orbit changing shape.

The right panel of figure D1 shows a stronger and more monotonic dependence of T_{cad} on $t_{\text{spin}}/t_{\text{orbit}}$. It appears that even slightly slower orbits sharply increases T_{cad} . This effect is both due to the asteroid spending greater time in the high-torque, near-perigee region, and the larger data set that can be collected for slow orbits. However, if the orbit speed is changed by adjusting its parameters (v_{∞} , r_p) or the central body mass μ_B , then the orbit shape will also change. This induces other effects studied in the main text and will complicate the trend observed here. Unlike the P_{ω} case, the cadence cut-off does not visibly broaden as a function of $t_{\text{spin}}/t_{\text{orbit}}$. It appears that the increased orbit speed merely shifts T_{cad} rather than changing its sharpness.

APPENDIX E: UNCERTAINTY DEPENDENCE ON ENCOUNTER PROPERTIES

JTD: Review after thresholds.

In this section, we investigate in greater detail the data presented in section 4.1 of the main text.

E1 Orbital elements

A Keplerian orbit is completely described by five parameters, but three describe the orbit's orientation with respect to the central body. They are therefore redundant with the orientation of the inertial frame and we do not investigate them here. We parametrize the remaining two parameters by the perigee distance r_p and excess velocity v_{∞} . Fits of the type described in section 2.3 were run for many values of r_p and v_{∞} and the 1 and 2σ posterior uncertainties are displayed in figure 8.

Figure 8 demonstrates that posterior uncertainty follows a slight trend for uncertainty to increase with v_{∞} . This is likely due to the fact that larger v_{∞} leads to a faster and flatter orbit with less time spent close to the planet, where tidal torque is strongest. There are also comparatively large oscillations in the uncertainty, due to the orientation of the

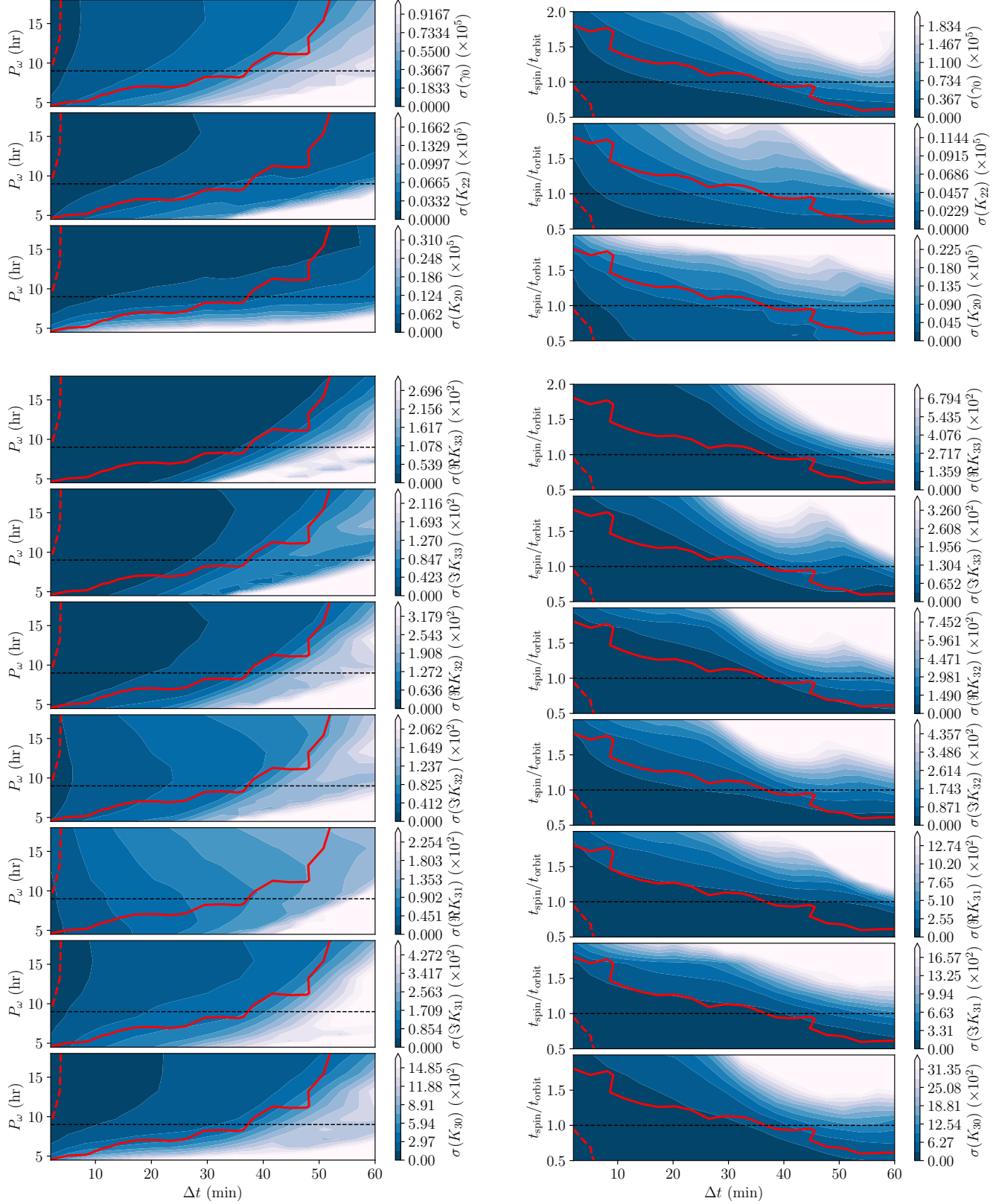


Figure D1. Contour plots showing posterior uncertainties as a function of cadence Δt and dynamical time scales for the encounter: rotational period P_ω (left) and the relative speed of the orbit (right; see text for a definition). The reference values of $P_\omega = 9$ hr and $t_{\text{spin}}/t_{\text{orbit}} = 1$ are shown as dotted lines. The solid (dotted) red line represents the $\sigma_\rho/\rho = 100\%$ (20%) threshold. Cadence cut-off depends strongly on both P_ω and $t_{\text{spin}}/t_{\text{orbit}} = 1$.

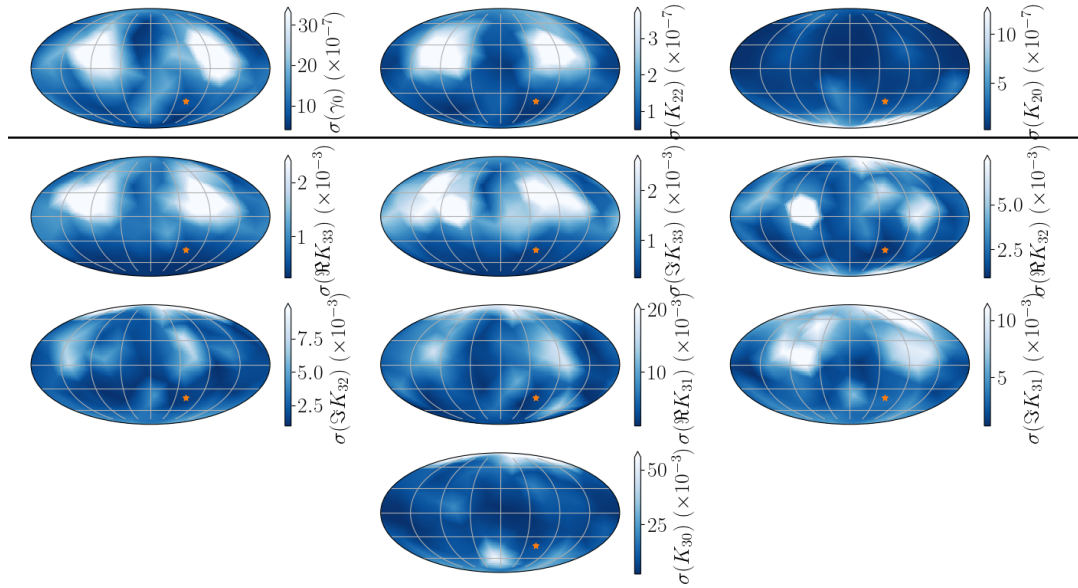


Figure E1. 1σ uncertainties for the first-order parameters (*top*) and second-order (*bottom*) as a function of the initial direction of spin in the inertial frame. All maps are made in the Mollweide projection. The orange star indicates the reference spin pole. The red contours enclose regions the 20% (dotted) and 100% (solid) σ_ρ/ρ cut-off. Posterior uncertainty depends similarly on initial spin pole direction for all parameters

asteroid at perigee varying. (The asteroid is always simulated to start at the same orientation, but increasing v_∞ decreases the time to perigee so that the asteroid enters this region of high torque at different orientations depending on v_∞ .) Hence, the oscillations have the same period for all parameters.

The figure shows much stronger dependence of parameter uncertainty on perigee distance, as expected by the factor of $(a_A/D)^{e'}$ present in equation 4 and mentioned in section A3. For $r_p = 7.9$ Earth radii, σ_ρ/ρ reaches the 100% threshold. The 20% threshold is reached at lower 4.7 Earth radii. Much of this uncertainty is dominated by uncertainty in K_{30} , which is the parameter least constrained by tidal torque analysis. At $r_p \approx 10$ Earth radii, K_{30} fills the prior distribution with uncertainty ranging from -1 to 1, visible by the sudden cut-off in uncertainty increase and the discontinuity of the $\sigma(K_{\ell m})$ curve there.

The axes of figure 8 show that parameters with large m are more precisely determined than parameters with small m , as can be seen by comparing K_{22} to K_{20} and comparing K_{33} to other K_{3m} values. Large m moments correspond to moments that control higher frequency fluctuations in density at the asteroid equator. This pattern of $\sigma(K_{\ell m})$ smaller for large m is a general trend and will be seen in the following sections as well.

The very strong dependence of $\sigma(K_{\ell m})$ on r_p makes this analysis most useful to extract second-order moments on close encounters. Fortunately, in the case of Earth, these encounters are also likely to have the best associated observational uncertainty when above the horizon due to their proximity. The first-order moments can still be extracted at much larger perigee distances in our model.

E2 Observational uncertainty

Two parameters, σ_θ and σ_ρ , govern the observational uncertainty of the data set. These parameters are defined in section 2.2; σ_θ represents the standard deviation of the angle between the true spin pole and the observed spin pole, while σ_ρ represents the standard deviation of the ratio between the observed and true rotational velocities. Rather than explore the full space spanned by these two values, we fix one and allow the other to vary to better assess whether uncertainty in spin pole or uncertainty in period more strongly affects posterior uncertainty $\sigma(K_{\ell m})$. This dependence is displayed in figure 9.

For the case in which σ_ρ is held fixed and σ_θ is varied, the figure shows that the dependence of $\sigma(K_{\ell m})$ on σ_θ is linear. The uncertainty threshold is reached at $\sigma_\theta = 2.8^\circ$ (0.5°) for $\sigma_\rho/\rho = 100\%$ (20%). The K_{2m} uncertainties remain low, even for $\sigma_\theta \approx 1$, which is large enough that the spin pole has non-negligible probability to be observed in any direction.

If σ_ρ is allowed to vary instead, then K_{30} reaches the 100% and 20% thresholds at σ_ρ which correspond to period uncertainty of several milliseconds. At large period uncertainty, the PPDs begin to fill the prior and the posterior uncertainty $\sigma(K_{\ell m})$ is no longer linear with σ_ρ (this is especially visible in the K_{30} case). Otherwise, posterior uncertainty is proportional to σ_ρ .

These data show that posterior uncertainty is extremely sensitive to observational uncertainty in period in our analysis. To precisely measure density moments, very accurate rotational period estimates would have to be made for every angular velocity data point. However this analysis does not study the effect of collecting more data after the encounter, or the correlations between different angular velocity measurements. If these correlations were taken into account, or

a more accurate uncertainty model used which took into account the asteroid's location in the sky or its distance to Earth, then the precision limit we find here will be affected.

E3 Asteroid shape

The true values of $K_{\ell m}$ and a_A , which quantify the asteroid's physical properties, affect the posterior uncertainties. Here, we only investigate the sensitivity of $\sigma(K_{\ell m})$ to the first-order parameters and a_A . These K_{2m} moments can also be viewed as the axes of a uniform density triaxial ellipsoid (equation A4).

In figure 10, we show the 1σ posterior uncertainties as a function of K_{20} and K_{22} , or alternatively a/c and b/c . We use axis ratios rather than the values of a , b , and c because axis ratios are independent of a_A . The large $|K_{22}|$ sides of the K_{2m} -space plots correspond to asymmetric ellipsoids, as do the points far from the $a/c = b/c$ diagonal of the axis-ratio-space plots. The point corresponding to a sphere, which experiences no tidal torque and no tumbling, is at $K_{2m} = 0$ and $a/c = b/c = 1$.

The figure shows large uncertainty in γ_0 for $K_{22} = 0$, or $a/c = b/c$, because K_{20} is rotationally symmetric around \hat{z} , and γ_0 is the initial orientation with respect to the \hat{z} axis. The system then has no dependence on γ_0 when $K_{22} = 0$. This induces degeneracy in the model which inflates uncertainties, not only in γ_0 but also the other components.

To remove the inflated uncertainty, one could assume a rotationally symmetric asteroid, remove γ_0 as a parameter, and run a fit. For a nearly rotationally symmetric asteroid however, a new parametrization is necessary which does not contain the ill-constrained γ_0 parameter. This task is beyond the scope of this paper, so we mostly consider asymmetric asteroids throughout.

Figure 10 also shows low uncertainty for highly asymmetric asteroids, where b/c and a/c are very different (i.e., when $|K_{22}|$ is large). Additionally, $\sigma(K_{20})$ and $\sigma(K_{22})$ decrease for large $|K_{20}|$, which corresponds to large axis ratios in the ellipsoid case.

Figure E2 displays the correlation between the first-order parameters. They show that γ_0 and K_{22} are often correlated for asymmetric asteroids, while γ_0 and K_{20} are usually not. This is expected as K_{22} is dependent on the orientation of the asteroid and K_{20} is not. They also show that K_{22} and K_{20} are usually correlated, and that a/c and b/c are highly correlated. The latter is expected due to the $1/c$ dependence.

The fact that $K_{\ell m}$ are correlated indicates that, in order to correctly propagate density moment uncertainties to a density distribution, a full PPD is necessary. If only 1σ uncertainty intervals for each parameter were used, density distribution uncertainty would be overestimated. This full PPD is produced by our fit process, but only the 1σ uncertainties are displayed in this paper in most cases.

Overall, the variation in the uncertainties on K_{20} and K_{22} (the first-order density moments) is present but largely smooth across their allowed parameter space, as is their correlation. It therefore seems reasonable to use the asymmetric asteroid shape as a stand-in for an unknown's asteroid shape when simulating an encounter, as we do in this paper. The uncertainty then can be expected to differ across

other shapes by a factor of about two or less, as long as the degenerate, symmetric asteroid regime is avoided.

On the other hand, the posterior uncertainty of K_{3m} is much more strongly dependent on asteroid length a_A . Figure 8 displays posterior uncertainty $\sigma(K_{\ell m})$ as a function of a_A . As was mentioned in section A3, the K_{2m} parameters are insensitive to a_A since the a_A^2 term in τ (equation 4) cancels the a_A^2 in the MOI (equation 5). The K_{3m} uncertainty is strongly dependent on a_A for the same reason that it is dependent on r_p : the $(a_A/D)^{\ell'}$ dependence of equation 4. At $a_A \leq 1100$ m, $\sigma_\rho/\rho \approx 100\%$. However, the 20% cut-off is much lower, at $a_A \leq 180$. Figure 8 demonstrates why these cut-offs are so distant; for large a_A , uncertainty decreases slowly with length. Only for small lengths is the uncertainty very large. This behaviour indicates that the uncertainty threshold is unlikely to fall much below 180 m even if other properties of the encounter are adjusted.

For uniform density asteroids, large a_A is equivalent to large asteroid radius. In non-uniform density asteroids, large a_A can also be achieved by distributing the mass of the asteroid near the surface, because the r^2 term in the integrand of the definition of a_A causes the density of regions distant from the asteroid centre of mass to dominate a_A .

E4 Cadence

The time between observations of asteroid angular velocity, or cadence, may vary depending on the observational schedule of the observing telescopes and the path of the asteroid through the sky. We measure how the posterior uncertainty $\sigma(K_{\ell m})$ varies with cadence ranging from two minutes to one hour in figure 9.

Figure 9 displays little dependence of uncertainty on cadence Δt for $\Delta t \lesssim 40$ min. We also see flaring of uncertainty for very large cadence, largely driven by the paucity of data points. However, uncertainty dramatically increases for many parameters at about $\Delta t = 30 - 40$ min, a time scale which is likely characteristic of the asteroid system. We name this rough cadence limit T_{cad} . T_{cad} is also the location at which the $\sigma(K_{3m})$ threshold is crossed for all second-order moments except K_{30} , which exceeds the uncertainty threshold at $\Delta t \approx 5$ min.

We expect this T_{cad} to be a function of two dynamical time scales of the system: the rotational period of the asteroid P_ω and the dynamical time scale of the orbit (the latter can be estimated in multiple ways, since both r_p/v_∞ and $v_\infty r_p^2/\mu_B$ have units of time and may be relevant). How these time scales affect T_{cad} is discussed in appendix D.

Figure 9 shows that as long as $\Delta t < T_{\text{cad}}$ is achieved, the influence of cadence on σ is minimal, but shorter cadence leads to lower uncertainties.

E5 Perigee gap

In certain circumstances, spin data might not be able to be captured for a close encounter at perigee. The asteroid might dip below the horizon, or it might pass too close to the sun to be observed. Generally, angular velocity data can be collected when the asteroid is distant from the central body, where torque is low. There, the angular velocity evolution is dominated by torque-free precession dictated by the MOI

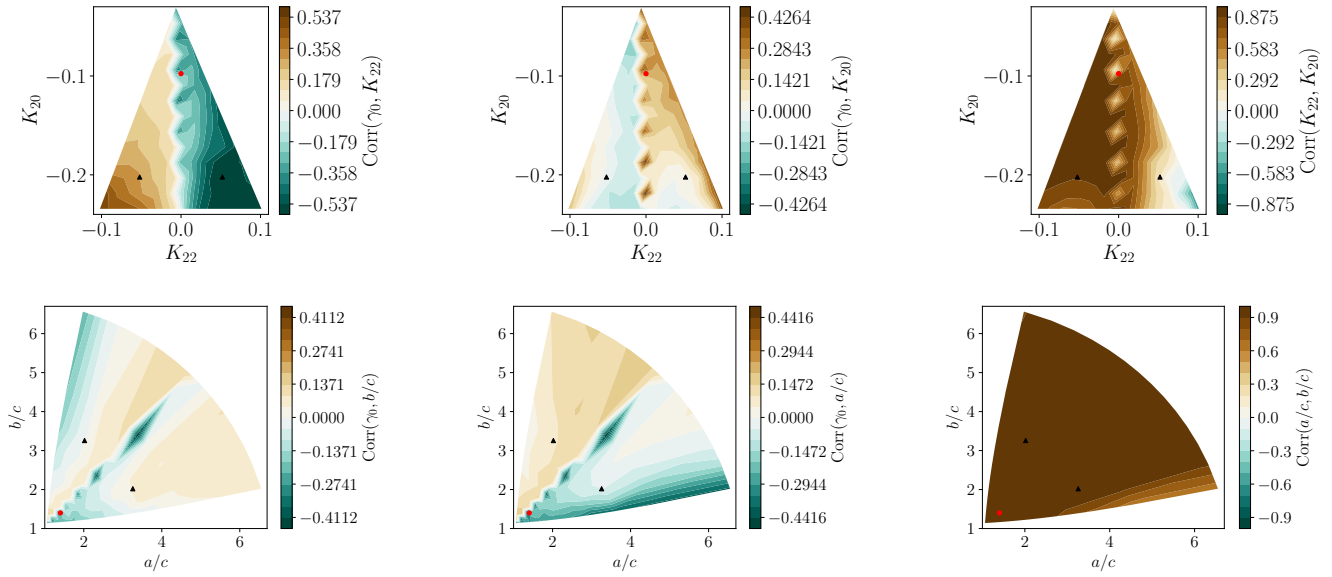


Figure E2. Correlations between PPDs for first-order parameters γ_0 , K_{22} , and K_{20} (top row) and γ_0 , a/c , and b/c (bottom row). Also shown as black points are the reference asteroid shapes: symmetric (red circle) and asymmetric (black triangle). The first order parameters K_{22} and K_{20} are correlated, as are initial orientation γ_0 and K_{22} .

components. That zero-torque data can still be used to fix K_{20} and K_{22} as in Moskovitz et al. (2020). However, K_{3m} does not affect the precession periods (though they do affect the phase). We are therefore curious as to how our posterior uncertainties change due to lack of perigee data.

To test this, we mask the perigee of the counter by removing a duration T_{gap} of data centred on the perigee, where T_{gap} ranges from 0 to 3 hours. To prevent lack of precision on $K_{\ell m}$ induced by lower amounts of data for high T_{gap} , we always cut 3 hr – T_{gap} from the data set, half from the beginning and half from the end, so that each data set produced for all T_{gap} has the same size. We then fit the same asteroid model to the cut data for all T_{gap} and plot posterior uncertainties $\sigma(K_{\ell m})$ in figure 9.

Since torque is greatest at perigee, we expect that region of the data to contain the most information about $K_{\ell m}$, and therefore uncertainty should increase monotonically with T_{gap} , which is seen in figure 9. We also see that the first-order parameters are not as sensitive to T_{gap} as the second-order parameters, because K_{2m} are additionally constrained by torque-free precession after perigee.

Most parameters show dramatically increased uncertainty in the $T \sim 1 - 2$ hr range. On the other hand, none of the uncertainties increase noticeably for $T \lesssim 1$ hr. Thirty minutes of dropped data is equivalent to fifteen dropped points for the simulated cadence of $\Delta t = 2$ minutes, showing that many data points can be dropped from the data set at perigee before the uncertainty starts to increase.

Qualitatively, 9 shows similar dependence of $\sigma(K_{\ell m})$ on T_{gap} as on cadence Δt ; they also both have cut-offs where uncertainty markedly increases, and both the T_{gap} and Δt cut-offs have qualitatively similar shapes although they occur at different values of Δt and T_{gap} . This suggests that the factors that govern uncertainty due to cadence also may govern sensitivity to lack of data at perigee in a similar way.

E6 Initial spin pole

The tidal torque experienced by the asteroid is affected by the initial direction of asteroid spin Ω_0 both because spin sets the initial asteroid orientation up to γ_0 and because of the spin-dependence of the rotational equations of motion (equation A14).

In figure E1, we display 1σ posterior uncertainties as a function of the direction of Ω_0 mapped onto the unit sphere in the inertial frame. Our samples for Ω_0 were laid out on a Fibonacci sphere to ensure they were roughly evenly spaced (marked in figure E3). To highlight common features across the parameters, we also display the average 1σ sensitivity in figure E3. The average is weighted such that the uncertainty map for each parameter contributes an equal amount (the weight of each map is set to one-tenth of the map's mean). This average map is presented in two different projections to allow data at \hat{Z} to be read.

Certain alignments of the body-fixed frame to the inertial frame lead to special conditions on torque, as discussed in section A3. For example, $z \parallel \hat{Z}$ and $z \parallel \hat{Y}$ at perigee lead to $\tau \parallel \hat{z}$ to first-order, and $\tau \parallel \hat{X}$ at perigee leads to $\tau = 0$ to first-order. We relate this to the initial direction of Ω_0 , via the approximation that τ is small until perigee. Then $\Omega_0 \parallel \hat{Y}$ and $\Omega_0 \parallel \hat{Z}$ both lead to $\tau \parallel \hat{z}$, and $\Omega_0 \parallel \hat{X}$ leads to $\tau = 0$.

Figure E3 shows areas of increased uncertainty for $\Omega_0 \parallel \hat{Z}$ and $\Omega_0 \parallel \hat{Y}$, but not the \hat{X} case. This indicates that $\tau \parallel \hat{z}$ causes increased uncertainty. Physically, $\tau \parallel \hat{z}$ only changes an asteroid's rotational period and does not cause it to tumble, eliminating the ability to discern MOI ratios from zero-torque precession after the encounter. If $\tau = 0$ to first-order, then second-order τ and non-perigee τ will dominate, which may increase precision to these usually non-dominant parameters and therefore not have the same increasing effect on $\sigma(K_{\ell m})$.

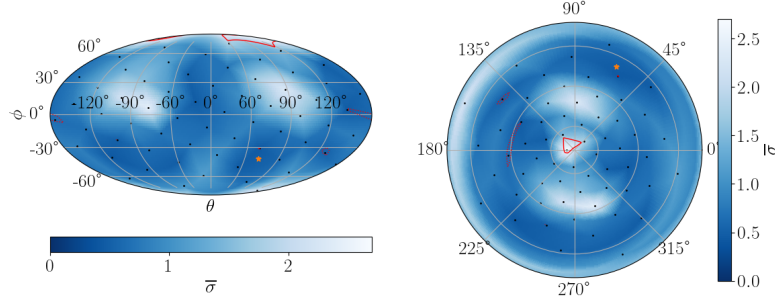


Figure E3. The weighted average of the uncertainties shown in figure E1, in Mollweide (left) and polar (right) projections in the inertial frame. See text for a description of how the average was computed. Black dots indicate the Fibonacci-sphere-distributed locations of sample spin poles, and the orange star indicates the reference spin pole. The polar projection is centred at the north pole, or $\hat{\mathbf{Z}}$. Posterior uncertainty is large near $\pm\hat{\mathbf{Z}}$ and $\pm\hat{\mathbf{Y}}$, but roughly constant elsewhere.

However, uncertainty does not vary by much more than a factor of two outside the imprecise regions of $\Omega_0 \parallel \hat{\mathbf{Z}}$ and $\Omega_0 \parallel \hat{\mathbf{Y}}$, though these regions are wide for some parameters. Within the imprecise regions, uncertainty can grow up to four times or more the uncertainty at other Ω_0 values, and can exceed the $\sigma(K_{3m}) \approx 0.01$ threshold. The trends for are roughly consistent across parameters (figure E1), leading to clearly visible imprecise regions in the average $\sigma(K_{\ell m})$ (figure E3).

E7 Rotational period

We also study the effect of the initial rotational period of the asteroid P_ω on posterior uncertainty $\sigma(K_{\ell m})$. In figure 8, we show $\sigma(K_{\ell m})$ as a function of P_ω for a range of periods typical of NEOs. Like figure 8, depicting the dependence of $\sigma(K_{\ell m})$ on v_∞ , figure 8 shows small-scale variation in uncertainty due to the fact that varying the initial period changes the value of γ at perigee, which affects uncertainty to a factor of about two. But a large-scale trend is also visible in many parameters. K_{20} and K_{22} show very large uncertainty for $P_\omega \lesssim 4$ hr because these fast-rotators tumble very little after perigee. This increases uncertainty on the K_{2m} parameters, which are constrained by tumbling.

We expect that quickly rotating asteroids would not tumble because, for small P_ω , the dynamical variables \mathbf{D} , $\boldsymbol{\omega}$, α , and β vary much smaller than γ . Approximating each variable as constant over one full rotation of γ , we can integrate the first-order contribution of $\boldsymbol{\tau}$ over $\gamma \in (0, 2\pi)$, which gives no secular, first-order torque to force the asteroid to tumble. However, this effect does not apply to the second-order parameters, since the integral over the second-order term of $\boldsymbol{\tau}$ does not vanish, as seen in the figure.

Another feature of figure 8 is that $K_{\ell 0}$ is more uncertain at low P_ω than the other parameters. This is most visible in the figure for K_{30} . The cause is likely that $K_{\ell 0}$ cannot contribute to τ_z as shown in equation 4. We already discussed that asteroids with small P_ω do not tumble, and since τ_x and τ_y are what induces tumbling, the most observable component of torque is therefore τ_z , which $K_{\ell 0}$ do not affect.

The most severe effect of period on $\sigma(K_{\ell m})$ is in the low-period regime ($P_\omega < 4.3$ hr), but in this case, the most strongly affected parameters are K_{2m} , which are generally known better than K_{3m} . The effect on the imprecise param-

eters K_{3m} is small, except for K_{30} . It therefore seems as though small-period asteroids are still candidates for observation, although high-period asteroids yield smaller uncertainty.

E8 Central body oblateness

In all the above studies, we assumed a spherical planet ($J_{\ell m} = 0$ for $\ell \geq 1$). By assumption that $\mu_B \gg \mu_A$ (so that the asteroid orbit's focus is the centre of mass of the central body), we have $J_{1m} = 0$. The effect of central body non-sphericity, then, is limited to the J_{2m} terms and damped by a factor of $(a_B/D)^2$. We expect these parameters to have small effect on the asteroid.

Here, we define oblateness as $\epsilon = (I_z - I_x)/(\mu_B R_B^2)$, where $I_{x,y,z}$ are the central body moments of inertia along the principal axes, and $I_x = I_y$. R_B is the true radius of the body (not a_B from equation A3).

$J_{\ell m}$ is defined in equation A3 with respect to the asteroid orbit, not the principal axes of the central body. However, for an equatorial orbit, the central body principal axes coincide with the asteroid orbit frame and we may express ϵ simply in terms of $J_{\ell m}$ as $\epsilon = -10J_{20}/3$ and $J_{22} = 0$. For simplicity, we use this equatorial orbit case. Since an oblate ellipsoid is mirror-symmetric around all three axes, table A1 indicates that J_{3m} are all zero. The next order of tidal torque is therefore J_{4m} , damped by an additional $(a_B/D)^2$ factor, and non-ellipsoid corrections to the central body shape. We do not consider these extra factors.

Given this conversion between ϵ and J_{20} , we analyze posterior uncertainty $\sigma(K_{2m})$ of the first-order parameters as a function of ϵ across a reasonable range of central body oblatenesses based on those of Solar System planets Pater & Lissauer (2015). These uncertainties are shown in the top panel of figure E4, together with linear best-fitting curves. The figure demonstrates almost no dependence of $\sigma(K_{\ell m})$ on oblateness ϵ , although posterior uncertainty does measurably decrease for oblate central bodies. The best-fitting lines match the uncertainties well, and they have slope of $[\Delta\sigma(K_{\ell m})/\sigma(K_{\ell m})_{\epsilon=0}]/\Delta\epsilon = -0.06$ for γ_0 , -0.2 for K_{22} , and -0.3 for K_{20} . The second-order parameters K_{3m} likely depend on oblateness similarly, but fitting these parameters is computationally more expensive and we do not study them.

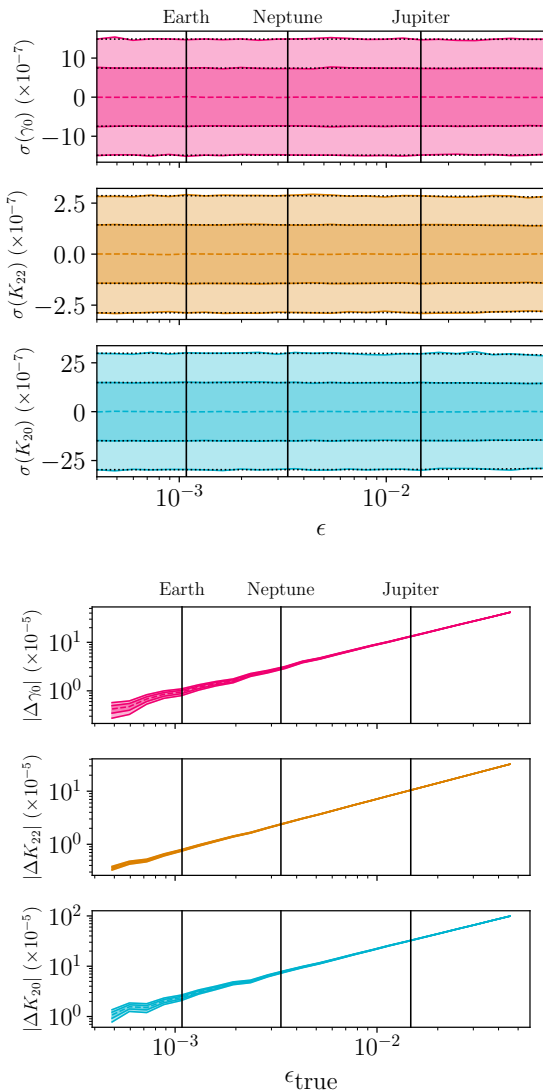


Figure E4. Top: 1 and 2σ confidence intervals for the first-order parameter PPDs as a function of oblateness ϵ . Linear best-fitting lines to $\sigma(K_{2m})$ (black, dotted) are plotted. Bottom: The difference between PPD means extracted from a zero-oblateness model and the true parameters given data with true oblateness $\epsilon_{\text{true}} \neq 0$. Also shown in both figures are the oblatenesses of reference Solar System bodies. Posterior uncertainty depends little on oblateness, but the best-fitting parameter estimates are affected enough by oblateness that oblateness must still be modelled.

Note that if an encounter is executed around one of the non-Earth objects noted in figure E4, a_B and μ_B will change in addition to ϵ . These two parameters also affect the posterior uncertainty (section 4.2), so the figure does not show that encounters with other bodies have the same precision as encounters with Earth; only that the difference in oblateness between the two bodies is of little concern.

Given the small effect of ϵ on $K_{\ell m}$, it might be tempting to neglect the planetary oblateness when fitting $K_{\ell m}$ to data. However, the bottom panel of figure E4 demonstrates that doing so is invalid. This figure displays $K_{\ell m}$ as extracted by a fit assuming $\epsilon = 0$, but run on data generated with non-zero ϵ . The difference between the PPD means and

true parameters are shown. Posterior uncertainties are also shown as bands. The figure shows that even for low (Earth-scale) oblateness, the fit results are inconsistent with the true $K_{\ell m}$ values, since $\Delta K_{\ell m} = 0$ is not contained in the 2σ band. This effect is much worse for large oblateness, growing to a difference on the order of $\mathcal{O}(100)\sigma$ for Jupiter's oblateness. Therefore, accurately modelling central-body oblateness to high precision is essential for accurate estimation of fit parameters. For non-equatorial orbits, with $J_{22} \neq 0$, we also expect J_{22} to affect the accuracy of the fit results to a similar degree, with the additional requirement of using the correct asteroid orbital plane.

J_{20} , the parameter studied in this section, has a slightly more general definition than oblateness. If the planet has a moon, the integral defining J_{20} (equation A3) can be extended to include this extra mass, though this can only be done when the asteroid never passes inside the moon's orbit. As an order-of-magnitude estimate for this effect, two spherical objects with masses and radii of Earth and the Moon, separated by one Lunar distance, and both lying in the orbital plane has a combined oblateness of $\epsilon = 0.82$. Extrapolating posterior uncertainties via the slopes of the best fit lines given earlier yields a reduction in $\sigma(K_{2m})$ by about 25%. Furthermore, J_{22} is non-zero for this case, which likely decreases posterior uncertainty even more.

This analysis suggests that large moons such as ours can improve fit quality, but further study of this effect is beyond the scope of this paper. Without a moon to inflate the oblateness of the central body, planetary oblateness does not significantly improve posterior uncertainty. However, correct representation of oblateness is essential to accurately estimate $K_{\ell m}$.

APPENDIX F: ANIMATED DENSITY DISTRIBUTIONS

This figure contains animations to better display the density distributions shown in the main text. Each frame represents a cross section perpendicular to the \hat{z} -axis, starting with negative z and ending with positive z .

This paper has been typeset from a TeX/LaTeX file prepared by the author.

Please see the published version of the paper for these animations, or find them online at the following links.

FE asymmetric density	FE asymmetric deviation	FE asymmetric uncertainty	FE asymmetric significance
FE symmetric density	FE symmetric deviation	FE symmetric uncertainty	FE symmetric significance
Lumpy asymmetric density	Lumpy asymmetric deviation	Lumpy asymmetric uncertainty	Lumpy asymmetric significance
Lumpy symmetric density	Lumpy symmetric deviation	Lumpy symmetric uncertainty	Lumpy symmetric significance

Figure F1. Density distributions extracted via the finite element model for the asymmetric (*first and third row*) and symmetric (*second and fourth rows*) reference asteroids. The finite element model (*top two rows*) and the lumpy model (*bottom two rows*) are employed. From left to right, the densities, deviations from the true density, uncertainties, and significance of the deviations are plotted. Animated form of figure 4.

Please see the published version of the paper for these animations, or find them online at the following links.

FE density	FE deviation	FE uncertainty	FE significance
Lumpy density	Lumpy deviation	Lumpy uncertainty	Lumpy significance

Figure F2. Density distributions extracted via the finite-element (*top*) and lumpy (*bottom*) models for an asteroid with a centred core. From left to right, the densities, deviations from the true density, uncertainties, and significance of the deviations are plotted. Animated form of figure 5.

Please see the published version of the paper for these animations, or find them online at the following links.

FE density	FE deviation	FE uncertainty	FE significance
Lumpy density	Lumpy deviation	Lumpy uncertainty	Lumpy significance

Figure F3. Density distributions extracted via the finite-element (*top*) and lumpy (*bottom*) models for an asteroid with an off-center core. From left to right, the densities, deviations from the true density, uncertainties, and significance of the deviations are plotted. Animated form of figure 12.

Please see the published version of the paper for these animations, or find them online at the following links.

FE density	FE deviation	FE uncertainty	FE significance
Lumpy density	Lumpy deviation	Lumpy uncertainty	Lumpy significance

Figure F4. Density distributions extracted via the finite-element (*top*) and the two-lump lumpy (*bottom*) models for an asteroid with two counterbalancing cores. From left to right, the densities, deviations from the true density, uncertainties, and significance of the deviations are plotted. Animated form of figure 13.